

1 **Response to reviewers comments**

2 We thank the reviewers for their comments. Below we detail our responses (in red) to each point raised.
3 Changes to the revised ms are listed in blue.

4

5 **1. Community Comment by Bill Lanyon**

6 Fault plane properties for United Downs case

7 The cohesion and frictional properties used describe the strength of intact rock specimens (from Elliott
8 1984). It seems very unlikely that a fault / fracture plane would have significant cohesion. Wouldn't it be
9 more reasonable to assume only frictional strength for fault planes?

10 **In general we agree, a fair point. However, in terms of the overall model for fracture susceptibility, we think**
11 **it is useful to include cohesion as a variable. We can run models for cohesion set to 0 to address this issue.**

12 **In terms of the fault zone itself, we haven't seen cuttings or core from the boreholes, nor outcrops of the**
13 **PFZ. So we don't know if this fault zone is best characterised in terms of fault core + fault damage, with**
14 **gouge and cataclasite in the core; or, if it is better considered as a fracture corridor of pre-existing joints**
15 **and veins. In the latter case, we might expect some, albeit small, cohesive strength (perhaps a few kPa). In**
16 **the former case, "strength" would be better captured as frictional strength. But there would then be a**
17 **dynamic aspect to that, beyond the simple Mohr-Coulomb analysis we have used (e.g., experimental**
18 **evidence for frictional strength increasing with longer hold times between slip events).**

19 **In the case of zero cohesion, the comments we make still stand: that our knowledge of friction coefficients,**
20 **and especially their statistical distribution - skewed high or low - could be better.**

21

22 I agree that it's potentially useful to keep cohesion in the formulation but using the intact rock values is just
23 going to significantly overestimate the fault plane strength at low normal stress. I don't think much data
24 has been released from the UD deep borehole yet, but for mechanical properties there's only side-wall core
25 and chippings both of which might be quite limited in providing frictional properties for fault planes at
26 seismic scales. The image logs probably give some guide as to the structure. So while it's nice to get more
27 data there will still be a lot of expert judgment on fault plane frictional properties that go into a pfs model
28 and "caution" is probably going to lead to using zero cohesion in many cases.

29 **OK, agreed.**

30

31 There is now some published information on the PTF at the UD site in a paper from Reinecker et al. in
32 Geothermics.

33 **We have read this paper and cite this in our ms.**

34 **Lines 394 and 397.**

35

36 **Response to Reviewer 1 – Jonathan Turner**

37 We thank the reviewer for their comments (repeated below in black) and provide detailed responses below
38 (in red).

39

40 This paper addresses a topic of general societal interest; it is well written, carefully explained, thoughtful.
41 The paper highlights the importance of several fault zone processes which are previously known about but
42 this study provides fresh perspective e.g. the role of uncoupled fluid pressure, coupled fluid pressure
43 (poroelasticity), the frictional properties of fault rocks (gouge, cataclasites), the importance of optimally
44 constraining in situ stress measurements, etc. In fact I think poroelasticity deserves wider discussion here
45 and elsewhere because it may be the key to understanding the unpredictability of induced seismicity.

46 We are pleased that the ms is considered to be well written, carefully explained and thoughtful.

47

48 I have few substantive comments and recommend that this paper be published.

49 Thank you.

50

51 1. It may be a bit too long with a little too much space devoted to explaining the method (or perhaps
52 consider cutting one of the two synthetic case studies).

53 OK, fair point (also made by Reviewer 2 – Anon). We will delete the Manchester coalfield case study and
54 focus on United Downs deep geothermal for fracture susceptibility and South Wales coalfield shallow
55 geothermal for slip tendency.

56 Section 3.2

57

58 2. Rangely oil field, Colorado is another good example to cite of a case study which showed a critical
59 threshold in fluid pressure, above which seismicity was induced and below which it was absent (sorry, I
60 don't have the reference but I think it was in the 1970s).

61 Good point. We will include this seminal study in our background and/or discussion.

62 Line 62.

63

64 3. The Townend & Zoback dataset is intriguing but in my experience very difficult to apply to development
65 projects. What I mean is that it is hard to demonstrate that critically stressed faults are
66 conductive/transmissive/higher perm, at least in as clearly as the T & Z dataset shows they should be.

67 Agreed. But tackling this is beyond the scope of our ms.

68

69 4. I got confused by the difference between slip tendency and friction coefficient – in words, friction
70 coefficient is the ratio of shear force to tractional force at the moment of failure. So I then thought it's no
71 surprise that your modal slip tendency in the first case study is 0.56 because that's the inverse tan of
72 ~30degree which is an 'average' angle of internal friction for compacted rocks. I would find it useful if this
73 point could be explained in slightly more detail.

74 Our understanding is that slip tendency is a feature of the stress field and the fault plane orientation (shear
75 stress/normal stress), whereas friction is a rock property (an empirical measurement from laboratory
76 tests). So if slip tendency exceeds friction, then a fault slips; if slip tendency is less than friction, there is no
77 slip.

78 The friction coefficient will vary for different lithologies, different fault rocks, slip rates, etc. So for recently
79 formed faults in the present day stress field, slip tendency ought to be about 0.6-0.85 (Byerlee). But that
80 does not have to be the case for “old” faults formed under different stress states, not least because the
81 orientation of the present day in situ stress is not the one at the time of faulting (e.g., Carboniferous or
82 Permian in the case of the UK coalfields).

83

84 **Response to Reviewer 2 – Anonymous**

85 We thank the reviewer for their comments (repeated below in black) and provide detailed responses below
86 (in red).

87

88 First of all, I would say that the authors are top scientists in this field and accordingly, the idea and the
89 methodology reported in this paper seem to be very promising. Moreover, for people like me with a
90 prevalent geological background, the pure statistical part of the paper can be hard to be read just because
91 of the background.

92 Thanks. One key aim of our ms (see lines 52 – 59) is to explain the underlying theory and statistical
93 background to the Response Surface Methodology for just these reasons. And according to Reviewer 1, it is
94 “well written, carefully explained and thoughtful”.

95 No change.

96

97 However, the geological data seems to be, in my opinion, poorly exposed here and the statistics are
98 sometimes completely detached from the geological data making this paper quite difficult to be read from
99 a Solid Earth reader.

100 We don’t understand what is meant by “geological data seems to be ... poorly exposed here”. We have
101 used the publicly available geological data for each case study, and cited all the sources.

102 Also, we do not understand the comment “the statistics are sometimes completely detached from the
103 geological data”. In the absence of complete certainty in the available data, we have used specific statistical
104 distributions to model the consequences of uncertainty.

105 No change.

106

107 Generally speaking, the paper faces a very interesting problem, and the method is innovative and very
108 exciting. As far as I can see the methodology is new and for this it must be tested and verified yet. The
109 authors attempt to do this by presenting two case studies with the aim to show “how combined RSM/MC
110 approach can be used to estimate the probability of slip on one or more faults”.

111 We agree that this is interesting, innovative and exciting.

112 No change.

113

114 However, the two cases are not very well constrained in terms of boundary conditions making the
115 probability estimation quite confused.

116 We do not understand what the reviewer means by “boundary conditions”. We are not conducting a
 117 numerical modelling analysis of a fixed spatial or temporal domain, e.g., of tensor fields or conservation
 118 equations using finite differences, and therefore the notion of formal boundary conditions is misplaced, in
 119 our opinion.

120 Our analysis, described in the first two sections, focuses on modelling the consequences of uncertainties in
 121 all of the possible input parameters involved in the quantification of fault stability (using either fracture
 122 susceptibility and slip tendency). As such it is a direct extension and development of the work presented by,
 123 for example, Chiaramonte et al. (2008) and Walsh & Zoback (2016). We do not think the probability
 124 estimation is “quite confused” (cf., comments by Reviewer 1).

125 No change.

126

127 Moreover, the two performed analyses (Porthtowan Fault Zone in Cornwall, UK and Coalfields in South
 128 Wales and Greater Manchester, UK) differ in so many aspects and, more importantly the presented results
 129 are different in terms of delivered outputs. This make the reading quite confusing and at the end of the
 130 paper I got lost about the point that the authors would like to address. In my opinion to test a new
 131 methodology we should apply this in areas where data are known as much as possible to see if the model
 132 prediction are reliable. In this case since the two areas are poorly constrained, this exercise is difficult to be
 133 followed and the results even more difficult to be understood.

134 We agree the case study areas are different, and the chosen modelled outputs are also different. This is all
 135 deliberate. Our intention is to demonstrate the scope of the method (combined RSM and MC) to make
 136 useful predictions about fault stability in terms of fracture susceptibility (United Downs) and slip tendency
 137 (coalfields) in the face of uncertainty.

138 As noted above in Response to Reviewer 1, we will remove the Manchester coalfield case study to reduce
 139 the length of the ms. We hope this makes it easier to appreciate the differences – and more importantly,
 140 the value in those differences – in the two case studies.

141 In relation to “we should apply this in areas where data are known as much as possible to see if the model
 142 prediction are reliable”: we know of no such datasets. In the case of United Downs – arguably one of the
 143 best constrained sites involved in geothermal energy – all of the data remain uncertain (to varying
 144 degrees), and this is one of our key points: even for areas with apparently “good” data, we argue that the
 145 existing uncertainties are significant and have consequences.

146 Section 3.2 has been reduced.

147

148 The discussion paragraphs more than discuss the results present a list of what we should know to better
 149 assess the seismic risk and the main message seems to be that we would need to know a lot of things. I can
 150 kind of agree with this but, once again, this makes the main message of the paper more confused.

151 We disagree with this comment and agree with Reviewer 1 that the ms is “well written, carefully explained
 152 and thoughtful”.

153

154 I strongly suggest the authors to simplify the paper in two ways.

- 155 1. Try to organize a sort of sensitivity analysis of the involved parameters in a more
- 156 structured and ordered way in order to facilitate the reader
- 157 2. Focus in one area and compare the results with something actually observed.

158 For the first point, sensitivity analyses are already included in the worked examples and in the case studies;
159 for example, we use CDF plots to explore the absolute sensitivity to selected parameters and we use
160 tornado plots to rank the relative sensitivities (see Figures 4, 5, 7 & 8).

161 For the second point, we think the reviewer might have missed the point. We know of no site or area
162 where the observations are known perfectly, i.e. with 100% certainty.

163 No change.

164

165 I think that we all agree that there are many topics related to the risk assessment (fault length, roughness,
166 friction, fluids, background seismicity, regional strain rate, and many many others) but in doing this exercise
167 authors must clearly state the assumption and critically analyze the results. In this paper I had the
168 impression that speaking about the many variables we lose the point of the paper, I would say that
169 sometimes less is more.

170 We have stated the assumptions used throughout (e.g., Mohr-Coulomb failure), and we critically analyse
171 the results through detailed statistical analysis of the outputs. One of our main aims, clearly listed in the
172 Introduction, is to provide a clear and detailed explanation of the method (in our opinion, so far lacking in
173 previous publications using similar methods). This entails some detailed and “careful explanation”
174 (Reviewer 1).

175 No change.

176

177 Minor points:

178 I am not so convinced about the statistical discussion that is sometimes too focused on the pure statistics
179 and few on the geology behind. For example, can we find a geological meaning to the “asymmetrical or
180 skewed” distribution of some parameters?

181 This is one of the issues raised by our ms, and clearly discussed! By trying to accommodate the fact of
182 uncertainty in all input parameters – stresses, orientations and rock properties – we are faced with making
183 choices about the nature (shape) of their distributions. We clearly state that there is currently insufficient
184 published data for many of these parameters – especially some critical ones such as cohesion and friction –
185 to find any “geological meaning”.

186 No change.

187

188 I Am not expert on Response Surface Methodology (RSM). However, the paragraph Statistical analysis of
189 geomechanical fault stability start with a discussion on the governing equations for RSM following a quite
190 long description that ends with the definition of Ts by meaning of the very well-known direction cosines
191 (e.g. Ramsay and Lisle 2000). In other word I can't really see why the authors need introducing the RSM
192 theory to infer the Ts definition.

193 The reviewer has perhaps missed the point. We are not “inferring” the Ts definition. The equations for Ts
194 are given in their full format (i.e., in terms of direction cosines) to highlight one of the key issues: there are
195 8 input parameters, and they are all, in general, uncertain. This is picked up in the succeeding paragraph
196 (line 221 in the original ms). We need to show the full equation for Ts before we make this crucial point.

197 No change.

198

199 A lot of acronyms BGS, CDF, are used but not defined. Even if they are quite easily understandable, this
200 gives the impression of a lazy writing

201 We presume the reviewer means “acronyms”. BGS is the British Geological Survey – we will add a definition
202 for that. CDF is defined on first use, on line 138.

203 BGS is now defined on first use in the main text, line 408.

204

205 The discussion on the relationship between fault length and events magnitude starts with this and ends
206 with discussing the relationship between fault length and number of events. I would say that the two
207 (maximum magnitude and number of events) are surely correlated but they are not the same thing.

208 Agreed. But we do not say they are the same thing.

209 No change.

210

211 Line to line comments:

212 Line 228 I would say that fluid pressure also influences Ts (e.g. De Paola et al., 2007)

213 We strongly disagree. Pore fluid pressure plays no part in the formal definition of slip tendency (Ts) – see
214 Morris et al., 1996. Moreover, the influence of pore fluid pressure on the potential for failure is better
215 understood in terms of fracture susceptibility – i.e., the pore fluid pressure increase needed to drive the
216 stress state on the fault to failure (Streit & Hillis, 2000).

217 No change.

218

219 Line 239 is CDF the cumulative distribution function? Authors should state this somewhere.

220 Yes it is. It is defined on first usage, on line 138 of the original ms.

221 No change.

222

223 Line 326 alfa has been not defined

224 Definition for alpha (α) will be added.

225 Now defined on first use, line 327.

226

227 Line 698 Why these may be the ones most likely to slip?

228 We are highlighting the *possibility* that unmapped (i.e., unknown) faults *may* be most likely – due to all the
229 factors discussed in this paper. The point is about unmapped faults, or so-called “known unknowns”.

230 No change.

231 Line 700 Some of this “mismatch” could be explained by the dip of the faults measured at the surface, but
232 not all. What the author mean here?

233 We mean that the surface traces of the faults shown on our maps may not coincide with their extension at
234 depth, e.g., for faults that dip at less than 90 degrees. This could explain some of the apparent mismatch
235 between the recorded earthquake locations plotted on the map relative to the surface traces.

236 No change.

237

238 Line 742 The observational record shows that bigger fault zones. I would say that there are a lot of physical
239 reasons behind this. Moreover, empirical relationships such as those suggested by Wells and Coppersmith
240 1994, or Leonard 2010 should be cited here.

241 Thanks for these suggestions. We will add these papers.

242 Line 810.

243

244 Subsequent comments and replies...

245 I read the answers to my comments, and I have to say that I really hope that the Editor and all the SE
246 readers will find the whole paper “well written, carefully explained and thoughtful” . I still think that some
247 parts should be improved, however I just reported my suggestions hoping to help.

248 In any case, I would like just to comment on the answer regarding Ts dependence on fluids.

249 The answer was:

250 We strongly disagree. Pore fluid pressure plays no part in the formal definition of slip tendency (Ts) – see
251 Morris et al., 1996[...].

252 In the Morris et al paper Ts is defined by τ/σ . σ are, generally speaking, the principal stresses
253 that might be interpreted as fluid pressure independent because effective stresses are not mentioned.
254 However, in the same paper, Morris et al., 1996 calculated the Ts for the Yucca Mountain area and, while
255 setting the input sigma, the literally write:

256 [...] to a depth of 5 km and assuming an average rock density of 2.7 g/cm³, $s_1 = 133$ MPa, $s_2 = 58$ – 108
257 MPa, and $s_3 = 63$ – 72 MPa. Assuming a water-table depth of 600 m (Stock et al., 1985), and
258 interconnecting permeability hydrostatic pressure at 5 km will be 43 MPa. Thus, effective principal stresses
259 would be: $s_1 = \text{vertical} = 90$ MPa, $s_2 = N258E-N308E = 45$ – 65 MPa (50%–72% of s_1), and $s_3 = N608W-N658W$
260 $= 20$ – 29 MPa (22%–32% of s_1), at 5 km beneath Yucca Mountain.

261 Please note that the effective stresses are those used by Morris et al., in their calculation of Ts (Figure 3).
262 This is also confirmed by Lisle and Srivastava, 2004 that literally write: “If pore-fluid pressures are involved,
263 then the stresses should be considered effective stresses.”

264 If effective stresses should be used, Ts would change with changing Pf, also because τ is Pore-pressure
265 independent. I would say, thus, that I “strongly” believe that Ts does depend on Pf.

266 What can be independent from Pf is the Ts/Tsmax ratio (defined as “T’s” by Lisle and Srivastava, 2004).
267 However, Ts and not T’s is investigated in the present paper by Healy and Hicks.

268

269 Thanks again for the comments.

270

271 We agree that the formal definition of slip tendency does not include pore fluid pressure. The question
272 then is: is it useful to modify the normal stress term by subtracting the pore fluid pressure to get an
273 'effective normal stress', and an 'effective slip tendency'.

274

275 In our opinion, the power of the original definition of Ts is how it can be related to the friction coefficient at
276 the fault surface. That is, the slip tendency, a function of the stresses on the fault plane, can be compared
277 to the rock properties (the friction coefficient), and an assessment of stability can be made. It is not clear
278 how this works for 'effective' terms. Effective friction?

279

280 Therefore, to clearly separate potential frictional processes from hydraulic (pore fluid pressure) processes,
281 we believe it is better to keep the original definition of slip tendency, and use fracture susceptibility as an
282 index of stability under effective pressure/stress.

283 No change.

284

285 **Response to Editorial comments by Federico Rossetti**

286 All formatting changes and typos have been corrected.

287 p17/1 – suggested move of paragraph. We disagree, as this section goes on to discuss linear and quadratic
288 response surfaces – which are not formally introduced until after line 538.

289 p17/2 – add unit of measure; the units in other plots are for fracture susceptibility (MPa), not for the
290 individual input parameters; slip tendency (as in this plot) has no units

291 p19/2 – same

292 p20/2 – deleted this line

293

294

295 De-risking the energy transition by quantifying the uncertainties in fault stability

296 David Healy¹ & Stephen P. Hicks²

297 ¹School of Geosciences, University of Aberdeen, Aberdeen AB24 3UE United Kingdom

298 ²Department of Earth Science and Engineering, Imperial College, London SW7 2AZ United Kingdom

299 d.healy@abdn.ac.uk

300

301 Abstract

302 The operations needed to decarbonise our energy systems increasingly involve faulted rocks in the
303 subsurface. To manage the technical challenges presented by these rocks and the justifiable public concern
304 over induced seismicity, we need to assess the risks. Widely used measures for fault stability, including slip
305 and dilation tendency and fracture susceptibility, can be combined with Response Surface Methodology from
306 engineering and Monte Carlo simulations to produce statistically viable ensembles for the analysis of
307 probability. In this paper, we describe the implementation of this approach using custom-built open source
308 Python code (pfs – probability of fault slip). The technique is then illustrated using two synthetic datasets and
309 two case studies drawn from active or potential sites for geothermal energy in the UK, and discussed in the
310 light of induced seismicity focal mechanisms. The analysis of probability highlights key gaps in our knowledge
311 of the stress field, fluid pressures and rock properties. Scope exists to develop, integrate and exploit citizen
312 science projects to generate more and better data, and simultaneously include the public in the necessary
313 discussions about hazard and risk.

314

315 Introduction

316 *Rationale & Objectives*

317 Faults in the crust slip in response to changes in stress or pore fluid pressure, and the source of these changes
318 can be either natural or anthropogenic. Estimating the likelihood of slip on a particular fault for a given
319 change in loading is critical for the industrial operations of the energy transition, especially geothermal
320 energy and carbon sequestration and storage (CCS). The target formations of these operations are nearly
321 always faulted and fractured to some degree, and experience from waste-water injection in the USA shows
322 how even small changes in pore fluid pressure can trigger frequent seismic slip on these faults, with
323 significant and widespread impact on society (e.g., Elsworth et al., 2016; Hincks et al., 2018; Hennings et al.,
324 2019).

325 Stephenson et al. (2019) have shown how quantitative analysis of the subsurface is one of the key
326 contributions that geoscientists can make to decarbonising energy production to meet national and
327 international targets (e.g., CCC, 2019; IPCC, 2018). This includes the systematic geomechanical
328 characterisation of rock formations, better understanding of fluid flow in fractured rocks, and the need for
329 pilot projects to explore the scaling of behaviours from the laboratory to the field. Perhaps the most
330 important aspect is to understand the public attitudes to subsurface decarbonisation technology
331 (Stephenson et al., 2019; Roberts et al., 2021). Several recent studies have addressed the uncertainties in
332 subsurface structural analysis of faulted rocks (Bond, 2015; Alcalde et al., 2017; Miocic et al., 2019). In this
333 paper, we extend this work to specifically include fault stability, and argue that in order to simultaneously
334 address public concerns and assess the viability of different schemes, we need a more rigorous approach to
335 risking subsurface decarbonisation activities, especially where these involve changes in load on faulted rocks.

336 Useful measures of fault stability include slip and dilation tendency (T_s and T_d respectively) and fracture
337 susceptibility (S_f , the change in fluid pressure to push effective stress to failure). These measures are defined
338 as functions of the *in situ* stress, the orientation of the fault plane and, in the case of S_f , rock properties. It is
339 widely recognised that the inputs for the prediction of stability are always uncertain, and to varying degrees:
340 e.g., the vertical stress component of the *in situ* stress tensor can often be quite well constrained (to within

5%) from density log data, whereas the maximum horizontal stress is generally much harder to quantify. To improve and focus our predictions of fault stability in the subsurface, we need to accept and incorporate these uncertainties into our calculations. In this paper, we describe and explore a statistical approach to fault stability calculations, and then apply these methods to examples in geothermal energy, in both low- and high-enthalpy settings.

The specific aims of this paper are to:

1. describe and explain the Response Surface Methodology, and show how it can be applied to the probabilistic estimation of fault stability using a range of different measures;
2. explore how the main variables – in situ stress, fault orientation and rock properties – relate to the different measures of fault stability (T_s , T_d and S_f) using synthetic (i.e., artificial) data;
3. use case studies of active and proposed geothermal projects with publicly available data to illustrate the method, and then highlight the relationships between our known but uncertain input data and the predicted risk of fault slip.

Importance & Previous work

Small changes in stress or fluid pressure (e.g., a few MPa) from human activities can have significant consequences for fault stability (Raleigh et al., 1976). For example, waste-water injection from hydraulic fracturing (“fracking”) operations has led to dramatic increases in seismicity in Oklahoma since 2009 (Hincks et al., 2018) and in Texas since 2008 (Hennings et al., 2019; Hicks et al., 2021). The precise mechanical cause(s) of this seismicity is the subject of some debate, and could be due to either ‘direct’ pore fluid pressure transfer to basement-hosted faults leading to a reduction in effective stress, or ‘indirect’ poroelastic effects at a distance (Elsworth et al., 2016; Goebel et al., 2019). The concept of critically stressed faults in the crust (Townend & Zoback, 2000), where relatively high permeability serves to maintain near-hydrostatic pore pressures, is consistent with the idea that only minor perturbations in loading can have dramatic consequences, even in areas of apparently low seismicity and, implicitly, low background tectonic loading.

In densely populated areas such as the UK, public support for, and confidence in, subsurface operations are key. Hydraulic fracturing operations for shale gas in Lancashire (UK) were stopped after earthquakes were triggered by fluid injection (Clarke et al., 2019). Triggered felt seismicity has already been reported at the United Downs deep geothermal pilot in Cornwall (Holmgren & Werner, 2021). Note that, in both of these cases, fracturing and/or fault slip are intrinsic to the success of the operation as they are needed to enhance fluid flow, and therefore earthquakes are inevitable. In detail, microseismicity (i.e., $M < 2$) is inevitable, but it is important to understand whether felt (i.e. $M > 2$) seismicity can be forecast ahead of time. Furthermore, many sites for energy transition projects in the UK are located in (beneath) areas of extreme poverty and social deprivation, both rural (e.g., Cornwall, South Wales) and urban (e.g., Glasgow), and therefore the risks from these projects fall disproportionately on the less well off (Nolan, 2016; McLennan et al., 2019). To begin to address these complex issues, we need to quantify which faults are more or less likely to slip in response to induced changes in loading. One approach is to analyse data during subsurface operations and attempt to manage the consequences (e.g., Verdon & Budge, 2018). An alternative approach, and the one taken in this paper, is to look at the bigger picture before operations commence and reduce risk from the outset.

Various measures have been proposed to quantify the propensity or tendency of a given fault to slip (or open) in a known stress field. The following methods are based around an assumption of Mohr-Coulomb (brittle-plastic) failure which has been shown to capture the key aspects of faulting in the upper crust. Slip tendency (T_s) was introduced by Morris et al. (1996) and is the simplest measure of fault stability, defined as:

$$T_s = \tau / \sigma_n \quad (1)$$

where τ is the shear stress and σ_n is the normal stress acting on the fault plane. These stress components in turn depend on the principal stresses and the orientation of the fault plane (see Lisle & Srivastava, 2004 for details). In the absence of cohesion, if the slip tendency on a fault equals or exceeds the coefficient of sliding friction, then the fault can be deemed “unstable”. This dimensionless index embodies the key mechanical principle underlying Mohr-Coulomb shear failure: as the shear (“sliding”) stress acting on a fault plane rises

in relation to the normal (or “clamping”) stress, the fault approaches failure and will slip. Slip tendency allows us to compare what we know about the stress state on a fault (τ , σ_n) with what we know about the rock properties (friction, μ). Dilation tendency (T_d) has been defined to describe the propensity for a fault to open, or dilate, in a given stress regime:

$$T_d = (\sigma_1 - \sigma_n) / (\sigma_1 - \sigma_3) \quad (2)$$

where σ_1 and σ_3 are the principal stresses of the *in situ* stress tensor (Ferrill et al., 1999).

Most rocks in the upper crust are porous and permeable to some degree, and fault rocks are no exception, so these rocks are generally fluid saturated. This implies that we should include pore fluid pressure and the concept of effective stress in our assessment of fault stability. Fracture susceptibility (S_f) is the change in pore fluid pressure needed to push a stressed fault to failure (Streit & Hillis, 2004) and is defined by:

$$S_f = \Delta P_f = (\sigma_n - P_f) - (\tau - C_0) / \mu \quad (3)$$

where P_f is the pore fluid pressure at the fault, C_0 is the cohesive strength (or cohesion), and μ is the coefficient of sliding friction (see Figure 1b).

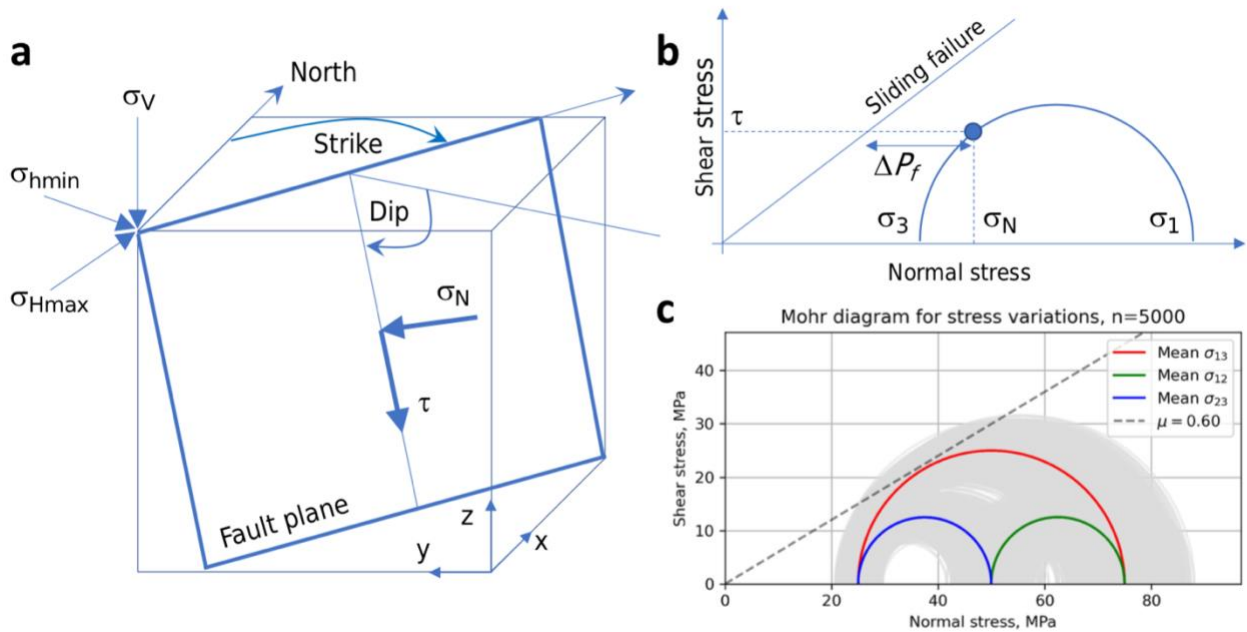


Figure 1. a. Schematic block diagram of a fault plane showing the terminology used in this paper. Also shown are the Cartesian and geographic reference frames and the Andersonian principal stresses. b. Mohr diagram for a given state of stress (blue semi-circle) with normal (σ_n) and shear stresses (τ) marked for a selected fault plane orientation (blue dot). Failure envelope for frictional sliding (cohesion=0) also shown as straight blue line. c. Mohr diagram depicting one of the key issues tackled in this paper: given uncertainty in the input stress values (grey Mohr circles for the variation around the average principal stresses in red, blue and green), what is the probability of failure? i.e., what percentage of all these stress states will intersect the failure envelope?

Previous applications of these three measures of fault stability – T_s , T_d and S_f – cover the full spectrum of rock types and stress fields, from basins to basement and from extensional, contractional and wrench tectonic settings. Applications within the domain of the energy transition include examples from geothermal energy (both shallow and deep) and CCS. The original definition of fracture susceptibility by Streit & Hillis (2004) was concerned with safe injection limits for CO₂ in potential reservoirs in Australia. Moeck et al. (2009) used slip tendency to quantify the relative stability of different fault sets in different horizons in a geothermal reservoir in the North German Basin, and Barcelona et al. (2019) used a similar method for Copahue geothermal reservoir in Argentina. For CCS, Williams et al., (2016, 2018) have used slip tendency analyses of faults in potential sandstone reservoirs on the UK continental shelf, including the North Sea and East Irish Sea basins.

420 The links between subsurface fluid flow, seismicity, and fault stability have recently been explored by Das &
 421 Mallik (2020) for the Koyna earthquakes in India, and by Wang et al. (2020) for strike-slip faults in the Tarim
 422 Basin of China.

423 Probabilistic approaches to fault stability have been adopted by various workers. In risking CO₂ storage for
 424 an oil reservoir in the Williston basin, Ayash et al. (2009) used a features, events and processes (FEP)
 425 approach to constrain the likelihood of occurrence of fault slip (based on slip tendency) and the severity of
 426 the consequences, with their product defined as the risk. Rohmer & Bouc (2010) used RSM to assess cap rock
 427 integrity for tensile or shear failure above deep aquifers in the Paris basin targeted for the storage of CO₂.
 428 Coupled RSM and Monte Carlo approaches to fault stability have been used by Chiamonte et al. (2008) and
 429 Walsh & Zoback (2016), following their initial application in the field of wellbore stability by Moos et al.
 430 (2003). This Fault Slip Potential (FSP) method developed by Stanford (e.g., Chiamonte et al., 2008 & Walsh
 431 & Zoback, 2016) calculates the response surface for fracture susceptibility, with the in situ stress tensor
 432 calculated by inversion of abundant seismicity data (focal mechanisms), and then uses a Monte Carlo
 433 simulation to generate cumulative distribution functions (CDFs) of conditional probability of slip defined with
 434 reference to an arbitrary pore pressure perturbation ($\Delta P_f = 2$ MPa, in the case of Walsh & Zoback, 2016).
 435 Note that FSP assumes cohesionless faults ($C_0=0$) and hydrostatic pore fluid pressure, and that *conditional*
 436 probability in this sense refers to the fact that we do not know where any particular fault is with respect to
 437 the seismic cycle.

438 *Conventions and layout for this paper*

439 In the sections below, we describe the underlying equations for measuring fault stability and then show how
 440 we can use Response Surface Methodology (RSM) from engineering to explore the consequences of
 441 uncertainties in the input variables. After assessing the quality of the solutions obtained from RSM, we then
 442 apply a brute force Monte Carlo (MC) approach to generate cumulative distribution functions (CDFs) of the
 443 different measures (T_s , T_d and S_f). The case studies use published, publicly available data to constrain the
 444 input variable distributions and then a combined RSM/MC approach is used to explore the uncertainty in
 445 fault stability in different settings.

446 In this paper, compressive stress is reckoned positive, with σ_1 as the maximum compressive principal stress
 447 and σ_3 as the minimum principal stress. Stress states and fault regimes are assumed to be Andersonian, with
 448 one principal stress vertical, although the underlying model and code could be changed to incorporate non-
 449 Andersonian stress states with the addition of extra variables for the stress tensor orientation (Walsh &
 450 Zoback, 2016). The likelihood of slip on a fault is assessed in the framework of Mohr-Coulomb failure, with
 451 or without cohesion (Jaeger et al., 2009). Fault orientations are quantified as strike and dip, following the
 452 right-hand rule: with your right hand flat on the fault plane and fingers pointing down dip, the right thumb
 453 points in the direction (azimuth) of strike. The relationship between the geographical and cartesian reference
 454 frames follows a North-East-Down convention. Figure 1 depicts the key terms and elements used in the
 455 analysis, and Table 1 contains a list of terms and symbols used with units where appropriate.

Quantity	Symbol	Units
Maximum compressive stress	σ_1	MPa
Intermediate compressive stress	σ_2	MPa
Minimum compressive stress	σ_3	MPa
Vertical stress	σ_v	MPa
Maximum horizontal stress	σ_{Hmax}	MPa
Minimum horizontal stress	σ_{Hmin}	MPa
Azimuth of max. horizontal stress	$sHaz$	0°-360°
Pore fluid pressure	P_f	MPa
Coefficient of friction	μ	dimensionless
Cohesive strength (or cohesion)	C_0	MPa
Slip tendency	T_s	dimensionless
Dilation tendency	T_d	dimensionless
Fracture susceptibility	S_f	MPa

Fault strike	φ	0°-180°
Fault dip	δ	0°-90°
Shear stress on a fault plane	τ	MPa
Normal stress on a fault plane	σ_n	MPa

Table 1. List of terms and symbols used in this paper, with units where appropriate.

Statistical analysis of geomechanical fault stability

Introduction to Response Surface Methodology (RSM)

RSM is widely used in engineering and industry along with a Design of Experiments approach, and often employed to optimise a specific process of interest – e.g., to maximise the yield of a reaction given the input variables of pressure, temperature, reactant mass etc. RSM is a large and growing field and is best considered as a toolbox of different methods with a common mathematical basis. The governing equations for RSM were derived by Box & Wilson (1951). The core idea is that a response y can be represented by a polynomial function of a number (q) of input variables $x_1 - x_q$:

$$y = f(x_1, x_2, \dots, x_q) \quad (4)$$

Each of the q input variables can be represented by either a discrete set of measurements made in the laboratory (or field) or drawn from appropriate statistical distributions (normal/Gaussian, skewed normal, Von Mises etc.). The simplest polynomial function that relates y and x is a linear one:

$$y_i = \beta_0 + \beta_1 x_{i1} + \beta_2 x_{i2} + \dots + \beta_q x_{iq} + \epsilon_i \quad (5)$$

$$y_i = \beta_0 + \sum_{j=1}^q \beta_j x_{ij} + \epsilon_i \quad (6)$$

where β_q are the coefficients (to be determined), y_i is the set of observations of the response ($i = 1, 2, \dots, N$), and x_{ij} are the input variables ($j = 1, 2, \dots, q$). ϵ is the experimental error, and the number of ‘observations’ $N > q$, the number of input variables. This is therefore a multiple regression model linking the response y to more than one (i.e., multiple) independent variables, x .

A more complex polynomial relationship is the quadratic form:

$$y = \beta_0 + \sum_{j=1}^q \beta_j x_j + \sum_{j=1}^q \beta_{jj} x_j^2 + \sum_{i < j}^q \beta_{ij} x_i x_j + \epsilon \quad (7)$$

This 2nd order multiple regression model contains all the terms of the linear (1st order) model, but also extra terms for the squares and cross-products of the input variables (second and third terms on the RHS of equation 7).

To define a response surface, either linear or quadratic, we need to calculate the values of the β_q coefficients. We can rewrite the key equations in matrix form:

$$\mathbf{y} = \mathbf{X}\boldsymbol{\beta} + \boldsymbol{\epsilon} \quad (8)$$

where \mathbf{y} is an ($N \times 1$) vector of observations (or calculations), \mathbf{X} is an ($N \times k$) matrix of input variable values ($k = q + 1$), and $\boldsymbol{\beta}$ is a ($k \times 1$) vector of regression coefficients. We solve this system of equations using the standard linear algebra technique of least squares regression (Myers et al., 2016):

$$\hat{\boldsymbol{\beta}} = (\mathbf{X}'\mathbf{X})^{-1}\mathbf{X}'\mathbf{y} \quad (9)$$

The response surface (linear or quadratic) is then defined by

$$\hat{\mathbf{y}} = \mathbf{X}\hat{\boldsymbol{\beta}} \quad (10)$$

The values used in \mathbf{X} are chosen to efficiently span the parameter space. A typical sampling design for \mathbf{X} is called the 3^q model with 3 values of each variable, usually the minimum, mean (or mode) and maximum. In

493 practice, coded variables are used in \mathbf{X} where the absolute values for the minimum, mean and maximum of
 494 each variable are scaled to -1 , 0 and $+1$ respectively, and then scaled back when the response surface is used
 495 in the Monte Carlo simulation (Myers et al., 2016).

496 The response surface – i.e., the set of β coefficients – is defined using a limited number of sample points,
 497 depending on the chosen sample design (3^q in the examples used in this paper; other variants exist – see
 498 Myers et al., 2016 for details). To explore the possible variations of a response more fully, we use a Monte
 499 Carlo (MC) approach of pre-defined size ($N_{MC} = 5,000$ in the examples in this paper). The MC simulation uses
 500 the response surface calculated from the design points to calculate the responses for N_{MC} combinations of
 501 input variables drawn from their distributions. This produces a statistically viable ensemble of response
 502 values from which we can infer the probability of the response with respect to a chosen threshold.

503 With respect to fault stability, we can use RSM to produce a parameterised relationship – the response
 504 surface in q dimensions – between a stability measure of interest and the q input variables. In the case of slip
 505 tendency T_s , we can rewrite the components of equation 1 in terms of the measurable input quantities as
 506 follows:

$$507 \quad \tau = \sqrt{(\sigma_1 - \sigma_2)^2 l^2 m^2 + (\sigma_2 - \sigma_3)^2 m^2 n^2 + (\sigma_3 - \sigma_1)^2 l^2 n^2} \quad (11)$$

$$508 \quad \sigma_n = \sigma_1 l^2 + \sigma_2 m^2 + \sigma_3 n^2 \quad (12)$$

509 where l , m and n are the direction cosines of the normal (pole) to the fault plane given by

$$510 \quad l = \sin \delta \sin \phi \quad (13a)$$

$$511 \quad m = -\sin \delta \cos \phi \quad (13b)$$

$$512 \quad n = \cos \delta \quad (13c)$$

513 where ϕ is the fault strike and δ is the fault dip, in a North-East-Down reference frame (Allmendinger et al.,
 514 2012).

515 All terms on the right-hand sides of equations 11-13 are uncertain to some degree, therefore estimating the
 516 uncertainty of T_s , and as importantly, the *key controls on the uncertainty of T_s* , in terms of these input
 517 variables, is non-trivial. This difficulty in estimating and visualising possible variations in our estimates of T_s
 518 is exacerbated by the recognition that each of the input variables may be distributed differently: some
 519 quantities (e.g., the principal stresses) may follow normal (Gaussian) statistics, whereas others (e.g., strike,
 520 dip, sHmax azimuth) will follow Von Mises distributions. In the case of fracture susceptibility (S_f , equation 3),
 521 it is even more complicated with the addition of three further input variables for friction, cohesion and pore
 522 fluid pressure. Measurements or calculations of coefficients of friction and cohesive strength often display
 523 asymmetric or skewed distributions (skewed high or low), and this adds further complexity to the task of
 524 estimating and constraining fault stability from the data at hand.

525 *Worked Example 1: Slip tendency from synthetic input data*

526 The calculations presented in this paper were all performed with the custom pfs (**p**robability of **f**ault **s**lip)
 527 package, written by the first author (DH) in Python 3, and freely available on GitHub (see Code Availability,
 528 below).

529 The first example calculates a response surface for slip tendency (T_s) from $q=6$ input variables: the
 530 magnitudes of the three principal stresses of the *in situ* stress tensor (σ_1 , σ_2 , σ_3) assumed Andersonian with
 531 one principal stress vertical, the azimuth of the maximum horizontal stress (*sHaz*), and the strike and dip of
 532 the fault plane. We build a response surface using a 3^q design, i.e., 3 data points for each variable – minimum,
 533 mean and maximum – and for T_s , $q = 6$. This means we calculate the response surface from $3^6 = 729$ data
 534 points. This response surface is then used in a Monte Carlo simulation ($N_{MC} = 5,000$) to generate a CDF of T_s
 535 values for the fault. The specific Python code to run this example in the pfs package is wrapped in a Jupyter
 536 notebook available on GitHub (WorkedExample1.ipynb).

537 The first task is to define the distributions of the input variables. In pfs, examples are shown for normal,
538 skewed normal and Von Mises (circular normal) distributions, but other statistical distributions are allowed.
539 Table 2 and Figure 2 describe the ranges and statistical moments of these distributions for each input
540 variable. For this example, the normally distributed principal stresses are defined with a variation (standard
541 deviation) of 5% of their central (mean) value, and the Von Mises distributions of the azimuthal variables
542 (sHaz, strike and dip) all have $\kappa = 200$ to model their dispersion about their mean. The fault of interest strikes
543 060° and dips 60° to the south (right hand rule). The key questions to be addressed by this example are:

- 544 1. given these uncertainties in the input stresses and orientation data, how does the estimation of T_s
545 vary? What is the range and the mode?
546 2. which variables exert the greatest (and least) control on the predicted variation in T_s ?

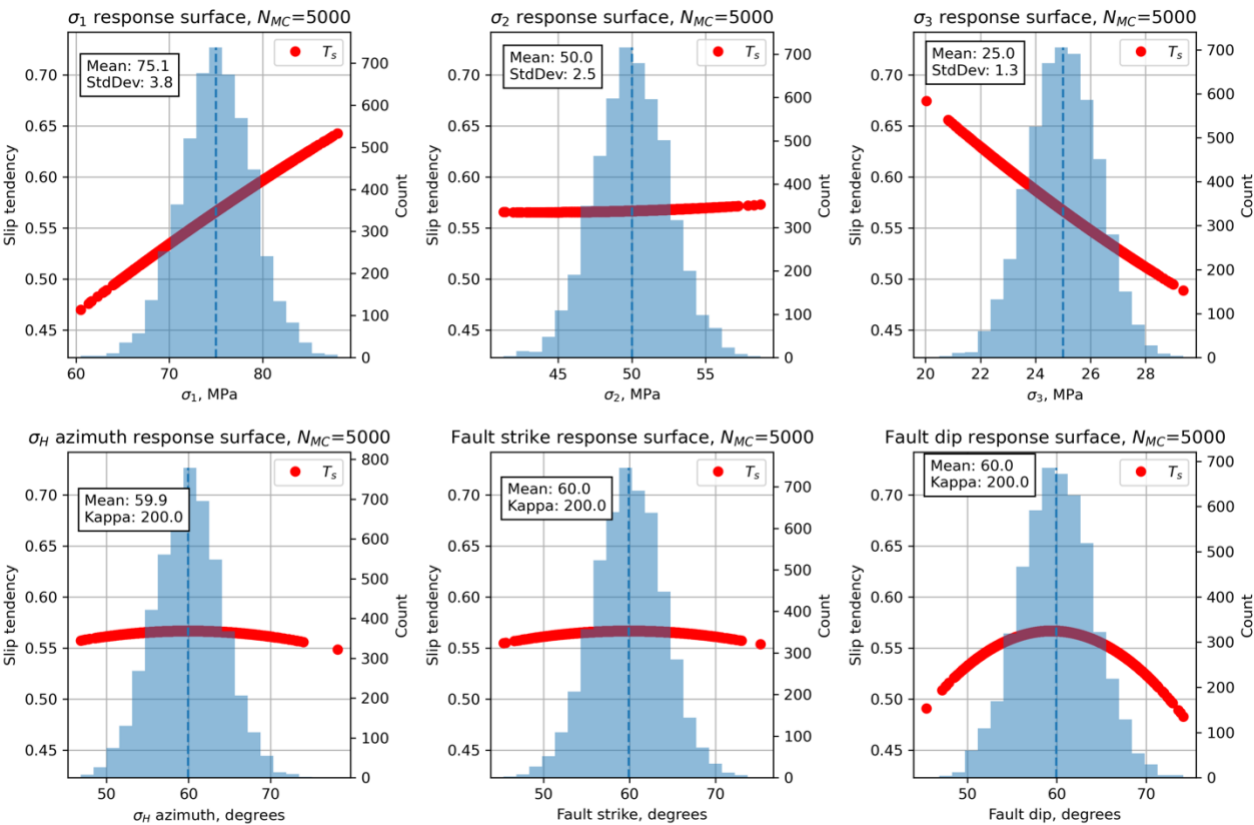
547 We compare a calculated linear response surface with a quadratic response surface, using a normal
548 probability plot of residuals (Figure 3). These residuals are the differences between the values of T_s derived
549 from the observations (taken from the input distributions shown in Table 2 (upper) and Figure 2), and the
550 calculated values of T_s using the β coefficients derived by least squares regression i.e., the response surface.
551 The adjusted R^2 value for the quadratic 2nd order model is significantly better than that for a linear 1st order
552 model, and we use quadratic models throughout the rest of this paper. More detailed inspection of the
553 quality of fit between the response surface and the observations is possible, including analysis of variance,
554 main effects plots and the use of t-statistics for each input variable to quantify their significance to the
555 definition of the β coefficients (Myers et al., 2016). In practice, visualising sections of the response surface
556 for individual variables is generally sufficient (see below; Moos et al., 2003; Walsh & Zoback, 2016).

Variable	Mean	Standard deviation (κ for Von Mises)	Units	Distribution	Comments
Worked Example 1 – Synthetic T_s – modelled depth=3 km					
σ_v , vertical stress	75.0	3.75 (5% of mean)	MPa	Normal	Lithostatic for depth of 3 km, assuming average rock density of 2500 kg m^{-3}
σ_H , max. horizontal stress	50.0	2.5 (5% of mean)	MPa	Normal	Andersonian normal faulting regime
σ_h , min. horizontal stress	25.0	1.25 (5% of mean)	MPa	Normal	
Azimuth of σ_{Hmax}	060	$\kappa=200$	$^\circ$	Von Mises (circular Normal)	
Fault strike	060	$\kappa=200$	$^\circ$	Von Mises (circular Normal)	
Fault dip	60.0	$\kappa=200$	$^\circ$	Von Mises (circular Normal), truncated at 0 and 90	
Worked Example 2 – Synthetic S_f – modelled depth=3 km					
σ_v , vertical stress	75.0	7.5 (10% of mean)	MPa	Normal	Lithostatic for depth of 3 km, assuming average rock density of 2500 kg m^{-3}
σ_H , max. horizontal stress	55.0	5.5 (10% of mean)	MPa	Normal	
σ_h , min. horizontal stress	35.0	3.5 (10% of mean)	MPa	Normal	

P_f , pore fluid pressure	30.0	3.0 (10% of mean)	MPa	Normal	Hydrostatic for depth of 3 km, assuming fluid density=1000 kg m ⁻³
Azimuth of σ_{Hmax}	060	$\kappa=200$	°	Von Mises (circular Normal)	
Fault strike	060	$\kappa=200$	°	Von Mises (circular Normal)	
Fault dip	60.0	$\kappa=200$	°	Von Mises (circular Normal), truncated at 0 and 90	
Friction, μ	0.6	0.12 (20% of mean)		Skewed normal	$\alpha = -3$ i.e., skewed low
Cohesion, C_0	20.0	2.0 (10% of mean)	MPa	Skewed normal	$\alpha = +3$ i.e., skewed high

557

558 **Table 2.** Table of input variable distributions for the synthetic models in Worked Examples 1 and 2.



559

560 **Figure 2.** Histograms of input variables used to calculate slip tendency (T_s) for the synthetic distributions
561 shown in Table 2 (Worked Example 1). Input value distributions are shown in blue. The calculated response
562 surface is shown in red.

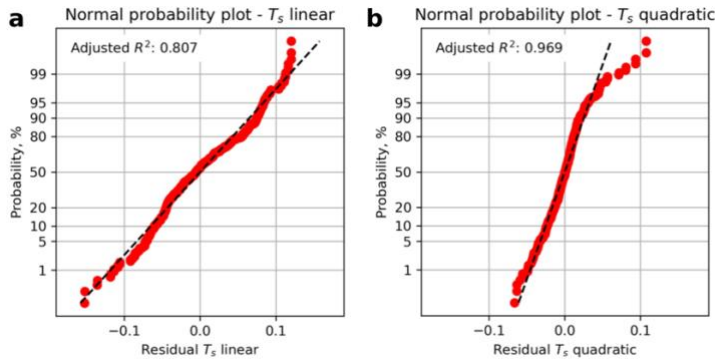
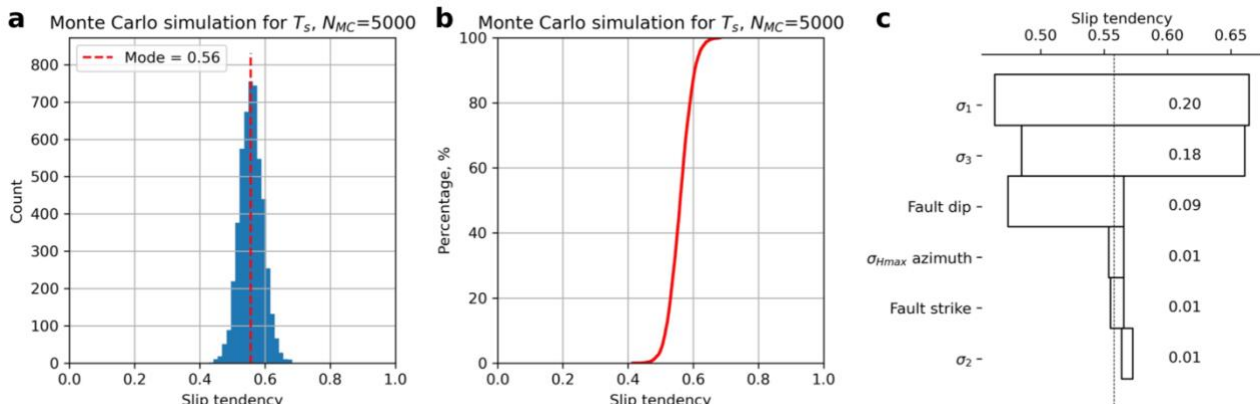


Figure 3. Residual plots for linear and quadratic response surfaces for slip tendency (T_s) using synthetic data from Worked Example 1. The quadratic fit has a higher value of the adjusted R^2 parameter and is therefore deemed better in this case.

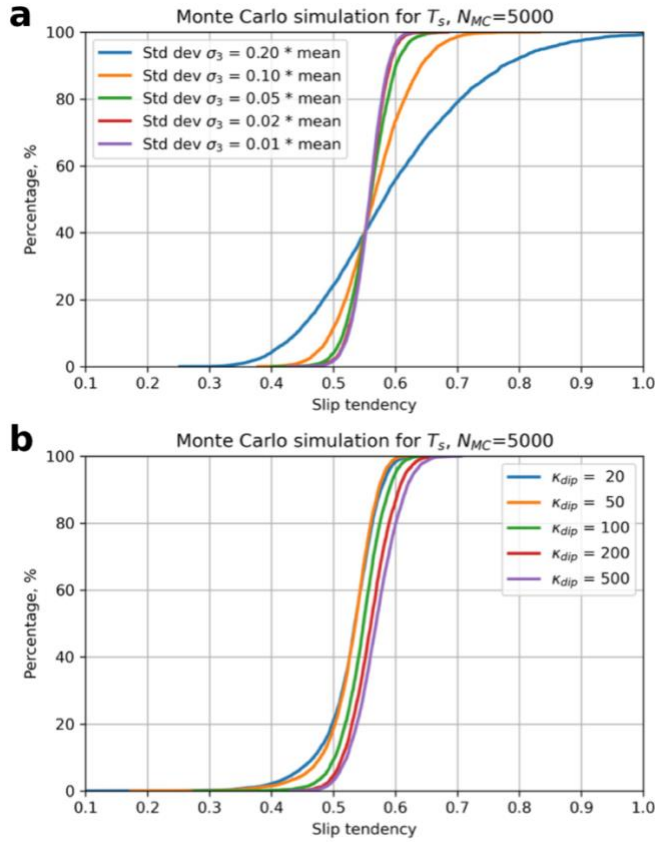
Having generated the quadratic response surface for T_s for these input distributions, we can now use it to perform a Monte Carlo (MC) simulation with the aim of generating a statistically viable ensemble from which we can infer the probability of T_s exceeding a critical value of sliding friction. The results from the MC analysis of T_s are shown in Figure 4. The histogram of all values of T_s shows a symmetrical and rather narrow distribution with a modal value of about 0.56 (Figure 4a). The CDF of all values of T_s also shows this narrow and symmetrical distribution (Figure 4b).

A response surface of more than two variables is not easy to visualise. One approach is to take sections through the surface at specific values of all but one variable and graph that. The red lines shown in Figure 2 depict the response surface for that variable with all other variables held at their mean values. Thus the red line in Figure 2a shows the variation in T_s as σ_1 varies with all other variables (σ_2 , σ_3 , $sHaz$, φ and δ) held at their mean values. There is a clear positive correlation of increasing T_s with increasing σ_1 , as expected from the definition of T_s and its underlying dependence on differential stress ($=\sigma_1 - \sigma_3$); the clear negative correlation of T_s with σ_3 shown in Figure 2c confirms this. Many of the response surface sections shown in Figure 2 are quasi-linear, but some are not: in particular, the dependencies of T_s on $sHaz$, strike and dip are all non-linear, and this further justifies the selection of a 2nd order quadratic response surface model.

A useful way to visualise the results from the response surface calculated by the MC simulation is the tornado plot shown in Figure 4c. Here the ranges of T_s for each input variable (shown as red lines over the histograms in Figure 2) are plotted to show the relative sensitivity of T_s to each variable. Variables are ranked from the largest range at the top to the lowest range at the bottom. Again, the core dependence of T_s on differential stress ($=\sigma_1 - \sigma_3$) is apparent, with σ_1 and σ_3 ranked highest in the plot. Interestingly, fault dip is ranked the next highest in terms of sensitivity and this reflects the geometry of this particular example. The Andersonian stress regime is for normal faulting, with σ_1 vertical. σ_2 is oriented parallel to fault strike ($sHaz$ = strike = 060°), and the fault dips at 60° . This fault is therefore ideally oriented for slip in this stress field. Small changes to dip will influence the ratio of τ to σ_n , and therefore T_s .



592 **Figure 4.** Output from Monte Carlo simulation ($N_{MC}=5,000$) of slip tendency (T_s) calculated using a quadratic
593 response surface from synthetic input data in Worked Example 1. **a.** Histogram of calculated T_s values, in this
594 case showing a quasi-normal distribution with a mode of ~ 0.55 . **b.** Cumulative distribution function (CDF) of
595 calculated T_s values, showing the range in values from ~ 0.4 to ~ 0.7 . **c.** Tornado plot showing relative
596 sensitivity to the input variables. The vertical dashed line shows the modal (most frequent) value of T_s from
597 the MC ensemble.



598 **Figure 5.** Output from Monte Carlo sensitivity tests for slip tendency, (T_s). **a.** Effect of variation in standard
599 deviation of the least principal stress, σ_3 . **b.** Effect of variation in dispersion (κ parameter of the Von Mises
600 distribution) of fault dip.
601

602 We can use a Monte Carlo approach to explore these sensitivities in more detail. Given the shape of the
603 response surface sections shown in Figure 2 and the ranking of variables in Figure 4c, we can quantify how
604 more or less variation in the inputs will affect the predicted T_s . Figure 5 shows the results of this sensitivity
605 analysis for σ_3 and fault dip. The most significant effect on the CDF of T_s is produced by increasing the
606 variation in σ_3 to 20% of the mean. This level of uncertainty for the minimum stress is not unreasonable in
607 real-world scenarios (see Case Studies below). Increased uncertainty in σ_3 at this level leads to a $\sim 20\%$ chance
608 of T_s being in excess of 0.7 ($p = 0.8$ for $T_s \leq 0.7$ from Figure 5a). Increased uncertainty in fault dip is achieved
609 by varying the dispersion parameter κ of the Von Mises distribution (lower values of κ = more dispersed).
610 Very disperse distributions of fault dip with $\kappa = 20$ only change T_s by < 0.1 .

611 *Worked Example 2: synthetic S_f*

612 We can explore variations in predicted fracture susceptibility using the same principles as for slip tendency,
613 but adjusted by incorporating three new variables as required by equation (3) – pore fluid pressure, friction
614 coefficient and cohesion (code in GitHub: WorkedExample2.ipynb). The number of variables q is now 9, and
615 therefore the design space used to compute the response surface is $3^q = 3^9 = 19,683$ data points. In practice
616 this means a slower run-time, but still only takes a few minutes on a modern processor.

617 For this example, we use the same stress tensor as for the T_s example, with σ_1 as the maximum principal
618 stress and vertical, i.e., an Andersonian normal fault regime for a depth of approximately 3 km. We constrain

the *in situ* pore pressure with a symmetrical normal distribution with a mean value of 30 MPa, which is approximately hydrostatic for a depth of 3 km, and with a variation of 10% of this mean. Friction is constrained by a skewed normal distribution with a mode of 0.56 and skewness parameter $\alpha = -3$, i.e., skewed towards lower values. This shape of distribution for friction coefficients is consistent with previous studies (e.g., Moos et al., 2003; Walsh & Zoback, 2016) but is open to question (see Discussion). Similarly for cohesion, we use a skewed normal distribution with a mode of 21 MPa and $\alpha = +3$, i.e., skewed towards higher values again consistent with previous work. These input variable distributions are documented in Table 2 (lower) and shown in the histograms of Figure 6.

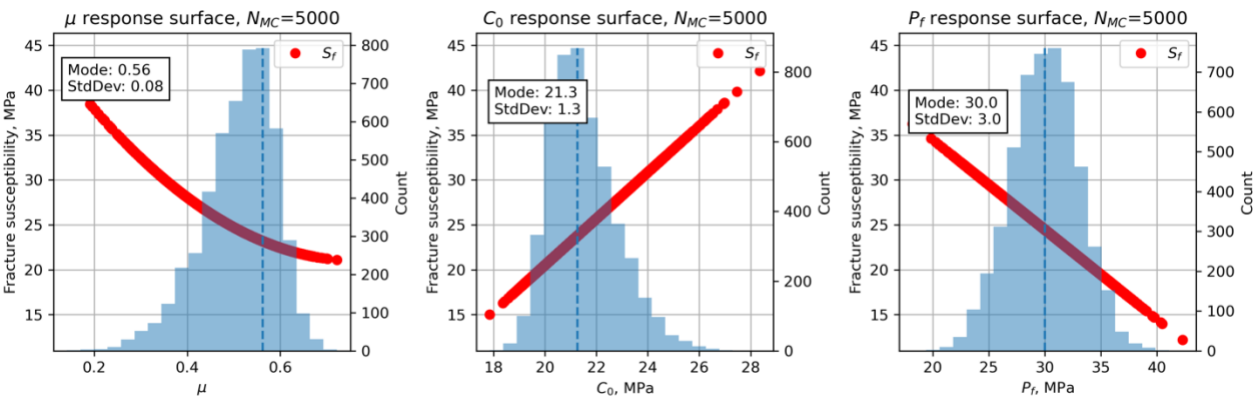


Figure 6. Histograms of the input variables (blue), in addition to those shown in Figure 2, used to calculate fracture susceptibility (S_f) for the synthetic distributions of Worked Example 2 shown in Table 2. Note the skewed (asymmetric) distributions for μ and C_0 .

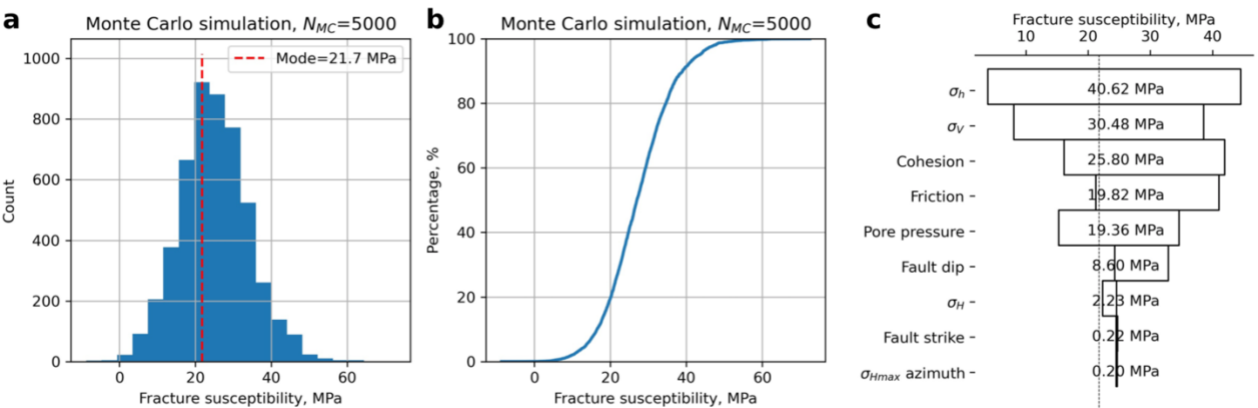
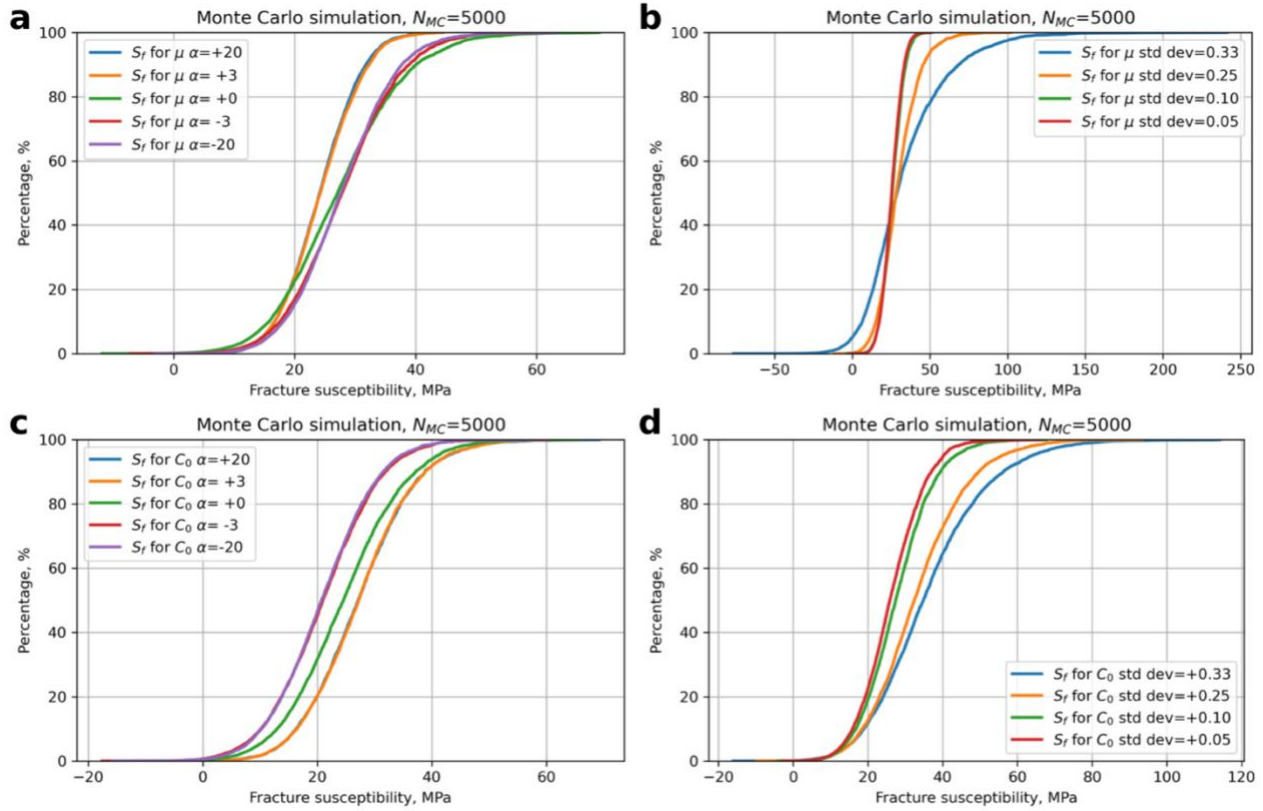


Figure 7. Output from Monte Carlo simulation ($N_{MC}=5,000$) of fracture susceptibility (S_f) calculated using a quadratic response surface from synthetic input data in Worked Example 2. **a.** Histogram of calculated fracture susceptibility, showing a quasi-normal distribution with a mode of 21.7 MPa. **b.** Cumulative distribution function (CDF) of calculated fracture susceptibility, showing the range in values from just less than 0 to about 60 MPa. **c.** Tornado plot of relative sensitivities of the input variables used to calculate fracture susceptibility (S_f).

We calculate a quadratic response surface and use a Monte Carlo simulation ($N_{MC} = 5,000$) to generate the ensemble summarised in Figure 7. The mode of the distribution of S_f is 21.7 MPa meaning that, on average, an increase in pore fluid pressure of about 22 MPa above the average *in situ* value of 30 MPa is needed to push the effective stress state to Mohr-Coulomb failure. The histogram in Figure 7a is approximately symmetrical, perhaps with a slight skewness to higher values, and this is reflected in the CDF shown in Figure 7b. The distribution is overwhelmingly positive, meaning that this fault is almost unconditionally stable for any change in pore fluid pressure, *at these conditions*. The response surface sections for μ , C_0 and P_f shown in Figure 6 (red lines) all show a strong influence on the fracture susceptibility, and these are confirmed in the tornado plot of Figure 7c. Pore fluid pressure exhibits a negative correlation with S_f (Figure 6c) which is

647 consistent with the general principle of effective stress: i.e., if the original *in situ* pore pressure is already
 648 high, it only takes a small perturbation (small $\Delta P_f = S_f$) to promote sliding failure. The response to changes in
 649 μ and C_0 is more interesting (Figure 6a and b). For this magnitude of cohesion, the effect of cohesion on S_f is
 650 greater than that of μ (C_0 ranks higher than μ in the tornado plot, Figure 7c), and the dependence of S_f on μ
 651 is negative. However, this relationship is not general as will be shown in the Case Study for the Porthtowan
 652 Fault Zone (see below).



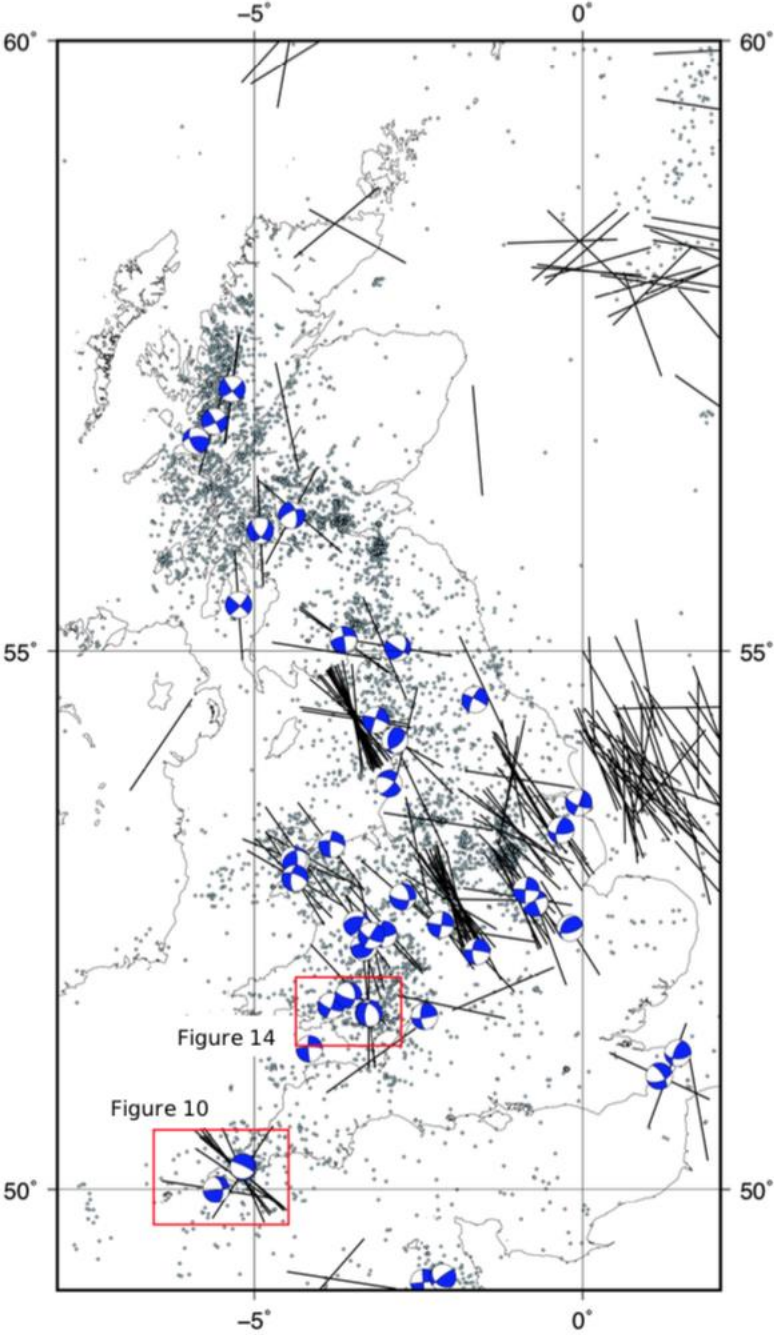
653
 654 **Figure 8.** Sensitivity of fracture susceptibility (S_f) to variations in μ and C_0 for Worked Example 2. Note the
 655 changes in scale along the x-axis between the plots.

656 The relative asymmetries of the skewed normal distributions for μ and C_0 have already been noted. Given
 657 their significant effect on S_f (high ranking in the tornado plot, Figure 7c), it is useful to explore how the
 658 *skewness* of these distributions might influence S_f . Figure 8 shows the results of repeated Monte Carlo
 659 sensitivity tests for μ (Figure 8a, b) and C_0 (Figure 8c, d). For friction, a positive skewness to higher values (α
 660 > 0) would tend to reduce S_f – i.e., faults would be less stable. For cohesion, the opposite is true – a negative
 661 skewness ($\alpha < 0$) would make faults less stable to changes in P_f . These asymmetries are opposite to the ones
 662 used in the main Worked Example 2 and used by other workers (see Discussion). Widening the distributions
 663 for μ or C_0 by increasing their standard deviations (and retaining the original α values) tends to broaden the
 664 distribution of predicted S_f with asymmetry to higher (i.e., more stable) values.

665 Case Studies

667 The case studies have been chosen to illustrate how a combined RSM/MC approach can be used to estimate
 668 the probability of slip on one or more faults. Selected specific aspects of the modelling and the visualisation
 669 of results are emphasised in each case study. Figure 9 shows a map of the UK with the case study areas
 670 marked, together with the locations of instrumentally-recorded earthquakes and their focal mechanisms
 671 (Baptie, 2010). Also shown are data from the World Stress Map database of 2016 (Heidbach et al., 2018)
 672 indicating the orientation of the maximum horizontal stress. A basic observation from this map is the level
 673 of complexity and heterogeneity in the present day seismotectonics of the UK, reflecting the variation in the

674 subsurface geology. However, there is a broad prevalence of NW-SE trending σ_{Hmax} directions and strike-slip
 675 earthquake mechanisms.

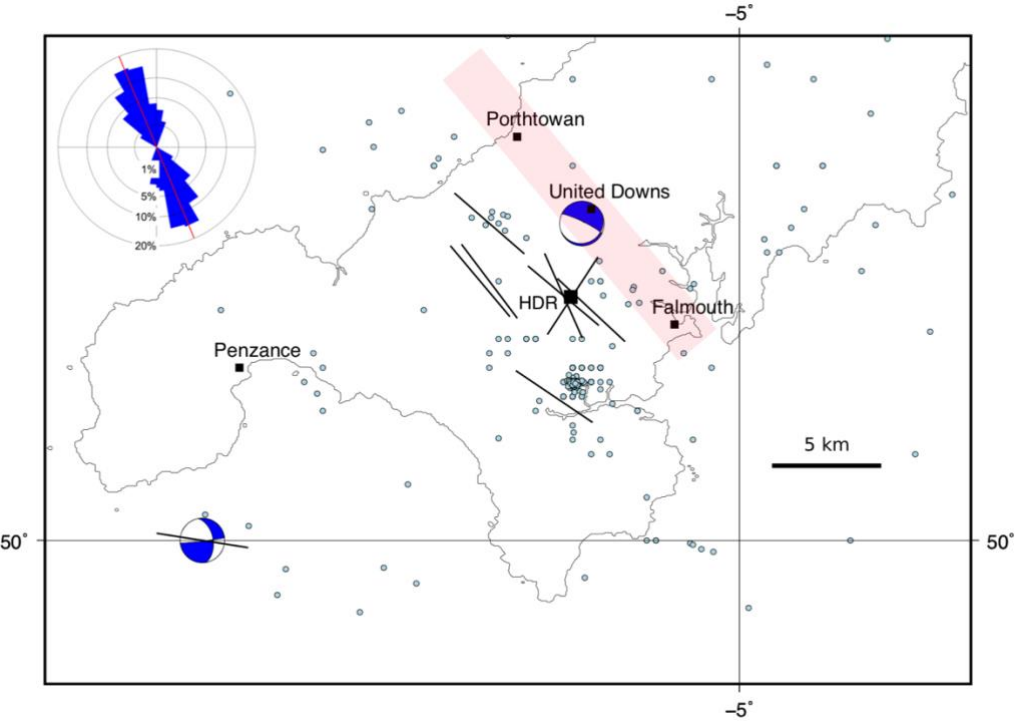


676
 677 **Figure 9.** Map of most of the UK showing the locations of the selected case studies (red rectangles). Also
 678 shown: epicentres of seismicity (light blue dots; British Geological Survey (BGS) catalogue – Musson, 1996),
 679 focal mechanisms (blue and white; Baptie, 2010), and orientations of the maximum horizontal stress (black
 680 lines; World Stress Map data – Heidbach et al., 2018).

681 1. *Porthtowan Fault Zone in Cornwall, UK*

682 The Porthtowan Fault Zone (PFZ) cuts the Carnmenellis granite in Cornwall in southwest England (Figure 10).
 683 This granite is a target for deep high-enthalpy geothermal energy due to its high radiogenic heat production
 684 (Beamish & Busby, 2016). Following the Hot Dry Rock (HDR) project in the 1980s (Pine & Batchelor, 1984;
 685 Batchelor & Pine, 1986), the United Downs pilot project has drilled two boreholes (UD-1, UD-2) to intersect
 686 the fault zone at depths of about 5,275 m and 2,393 metres, respectively, making UD-1 the deepest onshore
 687 borehole in the UK (Reinecker et al., 2021). The pilot project relies on shear-enhanced stimulation of pre-

688 existing fractures (joints, partially filled veins and faults) to drive fluid flow from the shallow injector (UD-2)
 689 to the deeper producer (UD-1). Temperatures at the base of UD-1 have been predicted at about 200°C
 690 (Ledingham et al., 2019), and recent observations confirm this (Reinecker et al., 2021). Shearing and
 691 downward flow of injected fluid was observed in boreholes as part of the earlier HDR project and tracked
 692 with measured microseismicity (Pine & Batchelor, 1984; Green et al., 1988; Li et al., 2018).



693
 694 **Figure 10.** Map of South West England showing: selected population centres, the United Downs deep
 695 geothermal pilot project and the former Hot Dry Rock project (HDR; black squares); epicentres of seismicity
 696 (light blue dots; BGS catalogue – Musson, 1996); focal mechanisms (blue and white; Baptie, 2010); and
 697 orientations of the maximum horizontal stress (black lines; World Stress Map data – Heidbach et al., 2018).
 698 Approximate trend and extent of the Porthtowan Fault Zone shown in pale red. Inset shows an equal area
 699 rose diagram with strikes of fault segments in the Porthtowan Fault Zone measured on British Geological
 700 Survey (BGS) Falmouth sheet 352 ($N=140$; circular mean strike= 158° , circular standard deviation= 27°).

701 The PFZ is poorly exposed inland, and runs NNW-SSE from Porthtowan on the north Cornish coast to
 702 Falmouth on the south coast (Figure 10; see inset rose diagram for strikes of constituent faults taken from
 703 the BGS Falmouth sheet 352). Overall, the fault zone is believed to dip steeply to the east at around 80° , but
 704 note that there is considerable variation in strike and dip of individual fault and fracture planes within the
 705 fault zone (Fellgett & Haslam, 2021). The azimuth of the maximum horizontal stress is broadly NW-SE, with
 706 one exception trending NE-SW.

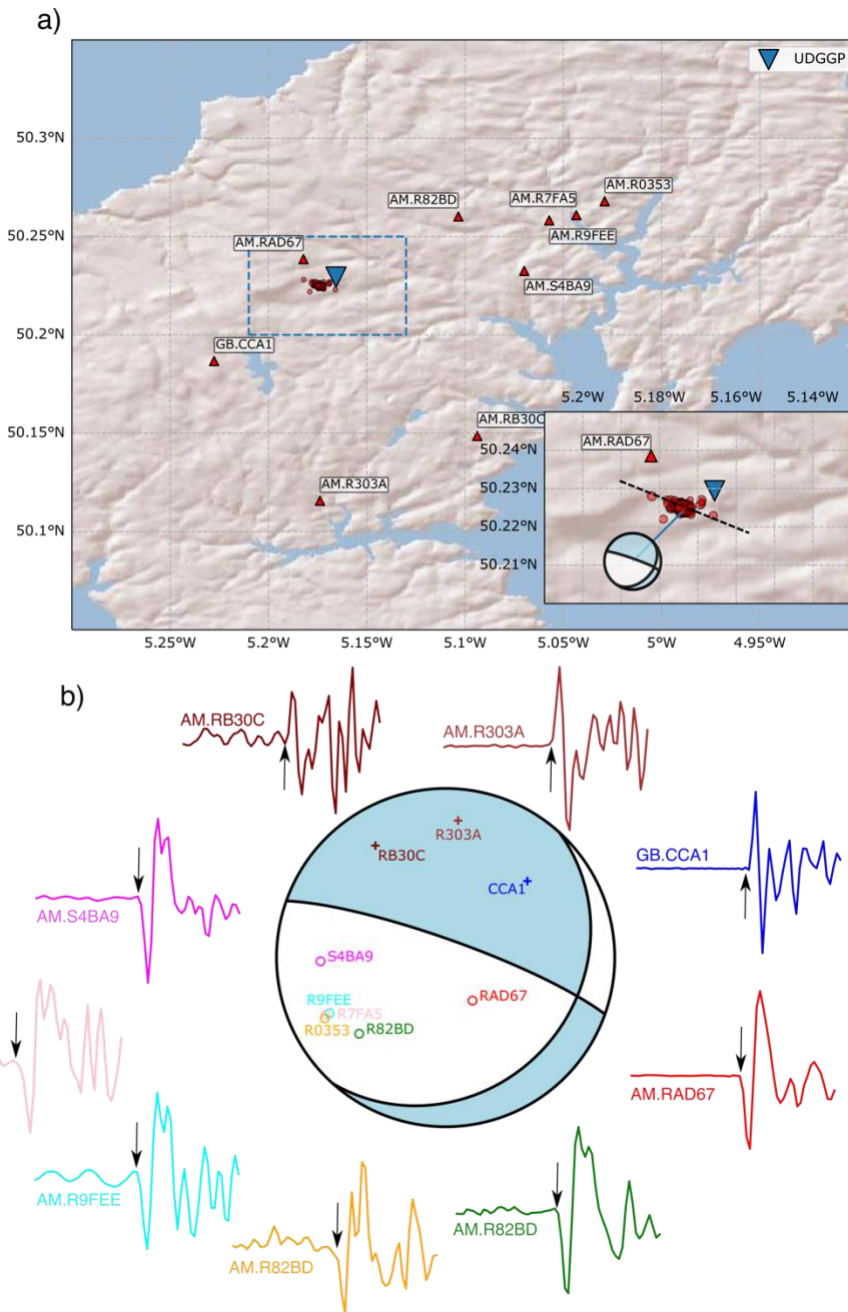
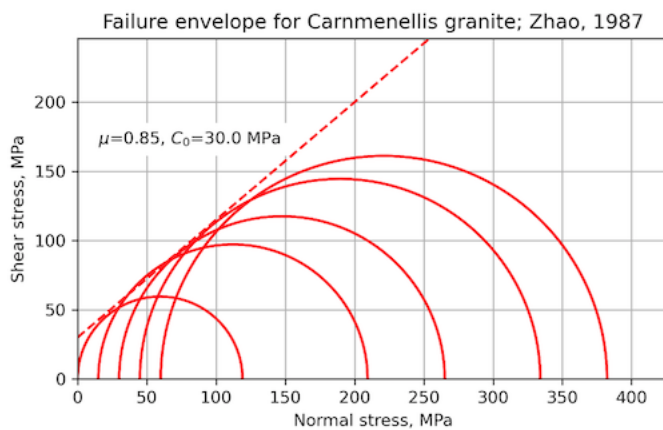
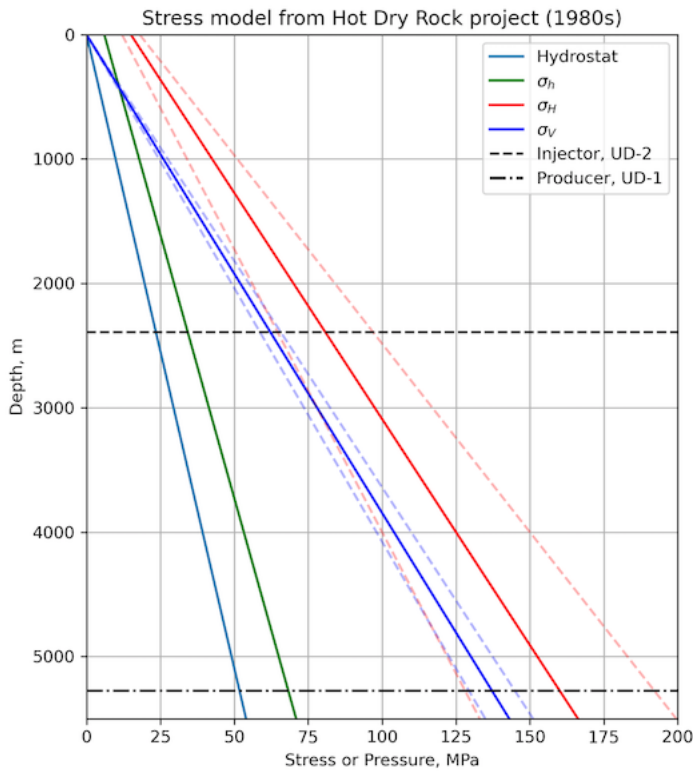


Figure 11. a. Red triangles show Raspberry Shake (network code: AM) and BGS (network code: GB) seismic stations in Cornwall, with station names labelled. Seismicity during geothermal operations is indicated by red circles. The inset shows a close-up of the area demarcated by the blue dashed line in the main map. The black dashed line in the inset shows the broad WNW-ESE alignment in seismicity. **b.** Computed focal mechanism for the 2020-09-30 11:44:01 M_L 1.6 induced earthquake. First-motions are plotted on the focal sphere with “+” indicating positive polarity, and “o” for negative polarities. P-wave first-motions are plotted starting and ending 0.3 seconds before and after the picked arrival, respectively, and are coloured in the same way as the points on the focal sphere.



717

718 **Figure 12.** Constraints on input variables for the Porthtowan Fault Zone modelling. **a.** Stress-depth plot based
 719 on data and equations from the Hot Dry Rock project in the Carnmenellis granite (Batchelor & Pine, 1986).
 720 Dashed lines show minimum and maximum values for each stress. Also shown are the depths of the two
 721 wells in the pilot project at United Downs. **b.** Mohr diagram showing data from laboratory mechanical tests
 722 of Zhao (1987) for brittle failure of Carnmenellis granite at 200°C. Estimated Mohr-Coulomb failure envelope
 723 (dashed red line) is defined by $\mu=0.85$, $C_0=30$ MPa.

724 Detailed geomechanical analyses were performed in the Carnmenellis granite in the 1980s as part of the HDR
 725 project, and these provide useful constraints on the variation of stress and fluid pressure with depth (Figure
 726 12a; Batchelor & Pine, 1986). From these data, a strike-slip regime is most likely with $\sigma_1 = \sigma_{Hmax}$ and $\sigma_2 = \sigma_v$,
 727 but note the uncertainties (based on quoted values in Batchelor & Pine, 1986): from around the depth of the
 728 injector well at United Downs and deeper, a normal fault regime is also consistent with the data, i.e., $\sigma_1 = \sigma_v$
 729 and $\sigma_2 = \sigma_{Hmax}$. Note that the earlier HDR project did not target a specific fault zone in the granite.

730 The thermo-mechanical properties of the Carnmenellis granite have been studied by Zhao (1987). Figure 12b
 731 shows a Mohr diagram of data taken from Table 2.3 of Zhao (1987) for laboratory brittle failure tests
 732 conducted at 200°C (the approximate temperature of the injector well at United Downs). From these data,

we have estimated a linear Mohr-Coulomb failure envelope defined by a friction coefficient of 0.85 and a cohesive strength of 30 MPa. Cuttings from the boreholes at United Downs have been used to measure friction coefficients of rocks within the PFZ, and values ranging between $\mu=0.28-0.6$ were recorded (Sanchez et al., 2020).

We present model results for fracture susceptibility in the PFZ as the plan at United Downs (and elsewhere in the future) is to inject fluid into the fault zone in order to generate shear-enhanced permeability on pre-existing fractures. Table 3 lists the input variable distributions used in the “base case” model for hydrostatic pore fluid pressure in the fault zone and mechanical properties taken from laboratory tests of intact Carnmenellis granite (Figure 12b). The modelled depth is chosen as 4 km, in between the depths of the UD-1 and UD-2 wells.

Variable	Mean	Standard deviation (κ for Von Mises)	Units	Distribution	Comments
σ_v , vertical stress	105.0	5.25 (5% of mean)	MPa	Normal	Lithostatic for depth of 4 km, assuming average rock density of 2650 kg m^{-3} Batchelor & Pine, 1986
σ_H , max. horizontal stress	125.0	25.0 (20% of mean)	MPa	Normal	Batchelor & Pine, 1986
σ_h , min. horizontal stress	53.0	5.3 (10% of mean)	MPa	Normal	Batchelor & Pine, 1986
P_f , pore fluid pressure	40.0	4.0 (10% of mean)	MPa	Normal	Hydrostatic for depth of 4 km, assuming average fluid density of 1000 kg m^{-3}
Azimuth of σ_{Hmax}	140	$\kappa=200$	°	Von Mises (circular Normal)	Batchelor & Pine, 1986
Fault strike	340	$\kappa=150$	°	As mapped	Digitised from BGS map
Fault dip	80.0	$\kappa=1000$	°	Von Mises (circular Normal), truncated at 0 and 90	
Friction, μ	0.85	0.17 (20% of mean)		Skewed normal	$\alpha = -3$ i.e., skewed low
Cohesion, C_0	30.0	6.0 (20% of mean)	MPa	Skewed normal	$\alpha = +3$ i.e., skewed high

Table 3. Distributions of input variables used in the base case model of fracture susceptibility (S_f) in the Porthtowan Fault Zone.

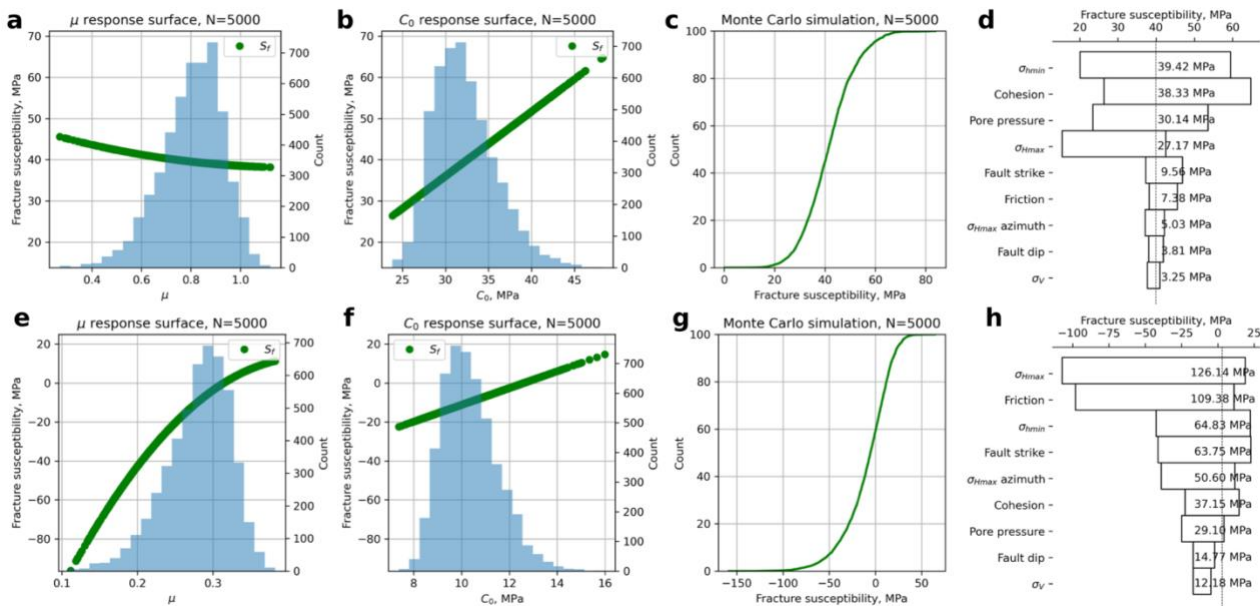


Figure 13. Outputs from the Monte Carlo simulation of fracture susceptibility (S_f) in the Porthtowan Fault Zone. **a-d.** The response surface for the base case, with friction and cohesion estimated from the laboratory failure tests of Zhao (1987), predicts positive fracture susceptibility i.e., a stable fault zone. The tornado plot (**d**) shows that for relatively high values of cohesion (mode of $C_0=30$ MPa in this case), the sensitivity to variations in friction is slight. **e-h.** In contrast, the response surface for the ‘weak fault’ case, with reduced values of friction and cohesion (mode of $\mu=0.3$, mode of $C_0=10$ MPa), predicts fault zone instability i.e., overwhelmingly negative values of S_f . The effect of friction on these predictions is now very strong, as shown in the shape of the response surface for μ (**e**) and in the ranking within the tornado plot (**h**).

The results from the Monte Carlo simulation of S_f for the PFZ are shown in Figure 13. For the base case, with hydrostatic pore fluid pressure and a ‘strong fault’ (mode of $\mu=0.85$, mode of $C_0=30$ MPa), the fault appears unconditionally stable for the modelled *in situ* stress variations. The CDF shows almost exclusively positive values of S_f up to about 60 MPa. Note that, for the input stress variations listed in Table 3, 22% of the MC simulations produced an Andersonian normal fault regime ($\sigma_1 = \sigma_V$), rather than a strike-slip ($\sigma_2 = \sigma_V$) regime.

232 microseismic events with hypocentre depths of 4-5 km were detected by the BGS during geothermal testing operations in 2021-2022 (http://www.earthquakes.bgs.ac.uk/data/data_archive.html; last accessed 23 July 2021). The largest earthquake induced by geothermal operations during this period occurred on 2020-09-30 11:44:01, and had a local magnitude of M_L 1.6, and was felt by residents in the area. This event was well-recorded on a network of single-component Raspberry Shake stations (e.g. Holmgren & Werner, 2021) and a single station of the BGS permanent monitoring network (Figure 11a). These stations offer excellent azimuthal coverage of the geothermal seismicity, with the closest station lying only 2 km away (AM.RAD67). Since no focal mechanisms have yet been documented for these induced earthquakes, we used recorded P-wave first motions to compute a focal mechanism of the M_L 1.6 event using the method of Hardebeck & Shearer (2002). Take-off angles were computed using a 1D seismic velocity model for the Cornwall area (<http://earthwise.bgs.ac.uk/index.php/OR/18/015> Table 4: Depth/crustal velocity models used in earthquake locations; last accessed 23 July 2021). The best-fitting focal mechanism (Figure 11b) indicates either normal faulting on a WNW-ESE steeply-dipping plane or strike-slip faulting on a shallow-dipping plane NE-SW striking plane. Single event relocated epicentres reported by the BGS, which use arrivals from a local dedicated microseismic monitoring array, show a NW-SE trend (Figure 11a), consistent with normal faulting on a steeply east-dipping, WNW-ESE striking plane during this earthquake. Negative P-wave polarities were recorded at AM.RAD67 for all $M > 0$ events, indicating that the same fault plane was likely reactivated during many of the induced events. The inferred fault plane is sub-parallel to the interpreted strike of the Porthtowan Fault Zone that is targeted by the geothermal testing. This observed normal faulting mechanism is consistent with our MC simulations (more than 1 in 5 of the predicted stress states were for normal faulting).

782 The response surface (green lines on Figure 13a-b) and the tornado plot of relative sensitivities of the input
 783 variables (Figure 13d) shows a positive dependence of S_f on the cohesion, and that variations in friction are
 784 relatively unimportant. If we reduce the strength of the modelled fault zone, by changing the input
 785 distributions of μ and C_0 to lower values – but with the same shape and skewness – the situation changes.
 786 The predicted fracture susceptibility is now much more strongly correlated with variations in friction, and
 787 less so with variations in cohesion. This can be explained by looking at the underlying formula for S_f (equation
 788 3), in particular the 2nd term on the RHS. If $C_0 > \tau$ then the numerator of this term can be negative, producing
 789 a net positive term. However, if $C_0 < \tau$ and μ is small then this term is larger and negative. The important
 790 point is that the probability distribution of S_f (compare Figure 13c and 13g) is controlled by the *relative*
 791 magnitudes of μ and C_0 . In a weak fault zone, with low μ and low C_0 , the predictions are very sensitive to the
 792 value of friction. In a strong fault, the effect of μ is less important. Thus, we need to know more about the
 793 relationship between μ and C_0 in fault rocks (see Discussion).

794 2. South Wales coalfield, UK

795 Scope exists to extract low enthalpy geothermal heat from disused coalmines in the UK (Farr et al., 2016),
 796 using either open- or closed-loop technology. Possible sites include the South Wales coalfield, where folded
 797 and faulted Coal Measures of Westphalian (upper Carboniferous) age have been mined for centuries, up until
 798 the 1980s. Initial plans for shallow mine geothermal schemes include *passive* dewatering which may not
 799 change the loading on faults by much. However, *active* dewatering schemes can promote ingress of deeper
 800 ground water (Farr et al., 2021), and as this fluid flow must be driven by gradients in fluid pressure, this could
 801 in turn lead to the instability of faults at greater depth. The models below are for a depth of 2 km.

802 The locations and orientations of faults have been taken from published BGS maps. We used the BGS
 803 Hydrogeology map of S Wales to map the traces of faults in the Coal Measures (Westphalian), and BGS 1:50k
 804 solid geology sheets over the same area to collect data on fault dips (Figure 14). Faults were traced onto
 805 scanned images of the maps in a graphics package (Affinity Designer on an Apple iPad using an Apple Pencil).
 806 These fault trace maps were saved in Scalable Vector Graphics (.SVG) format, after deleting the original
 807 scanned image layer of the geological map. The saved .SVG files were read into FracPaQ (Healy et al., 2017)
 808 to quantify their orientation distributions (inset rose plots in Figure 14a and b). The fault trace maps were
 809 then overlain on maps containing historical seismicity and available focal mechanisms (from the public BGS
 810 catalogue; Musson, 1996) and the orientations of σ_{Hmax} taken from the World Stress Map project (Heidbach
 811 et al., 2018).

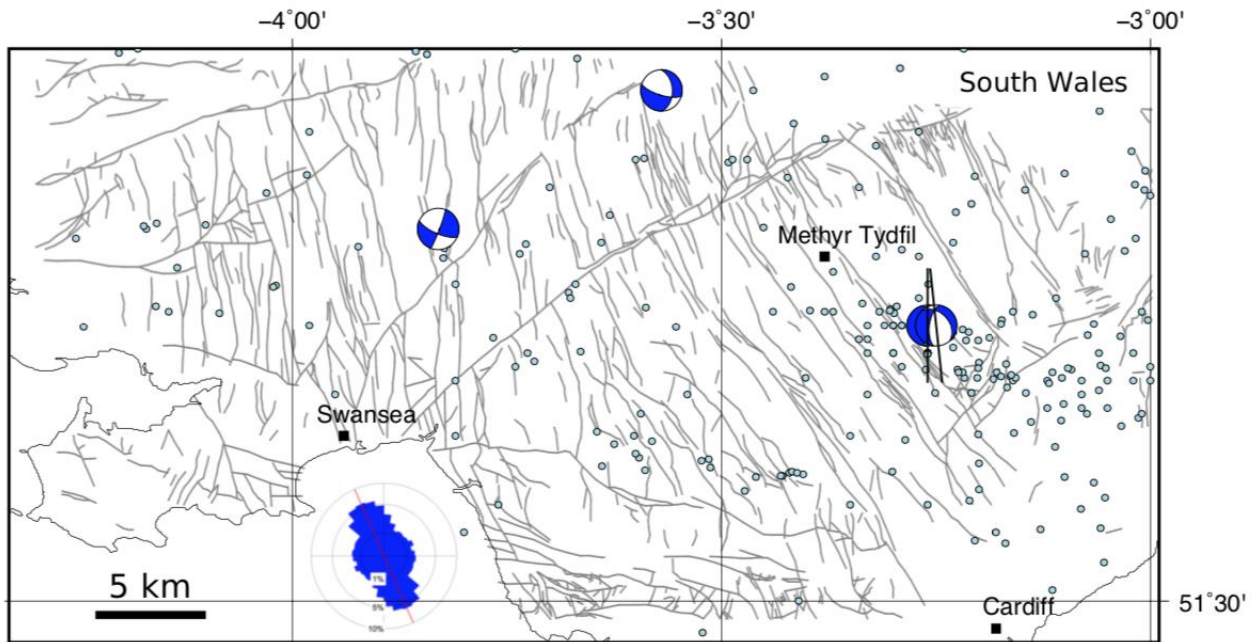
812 In the South Wales coalfield, 3,408 fault segments were traced, and the dominant trend is clearly NNW/SSE,
 813 but with important (and long) fault zones running ENE-WSW, such as the Neath and Swansea Valley
 814 Disturbances (Figure 14). From cross sections, we measured 142 fault dips to help constrain the distribution
 815 of friction coefficients in these rocks (Figure 15b-c; see below), corrected for vertical exaggeration on the
 816 section line where necessary. Focal mechanisms in this area ($n=4$) suggest that NNW/SSE and N/S faults are
 817 active in the current stress regime. Historical seismicity is widely, if unevenly, distributed with no obvious
 818 direct correlation to the surface mapped fault traces. For example, there are areas of intense surface faulting
 819 but no recorded historical seismicity, and vice versa – areas with abundant historical events but few mapped
 820 faults.

821 There are no published geomechanical analyses for the variation of stress with depth for this area. To
 822 constrain the depth dependence of stress, we have used larger scale syntheses of stress for onshore UK
 823 produced by the BGS (e.g., Kingdon et al., 2016; Fellgett et al., 2018). The stress-depth plot in Figure 15a has
 824 been constructed using the data shown in Fellgett et al. (2018), and shows that, in general, a strike-slip fault
 825 regime with $\sigma_1 = \sigma_{Hmax}$ is most likely. However, given the known uncertainties in these data, a normal fault
 826 regime ($\sigma_1 = \sigma_v$) cannot be ruled out, especially at depth. Note that the stress-depth data shown in Fellgett
 827 et al. (2018) and used in Figure 15a are compiled from different areas, and remain untested for the specific
 828 area shown in this paper. The azimuth of σ_{Hmax} is known to vary across the UK ranging from ~130 to ~170
 829 (Baptie et al., 2010; Becker & Davenport, 2001).

830 Despite the economic and historical significance of the Coal Measures, there are no published datasets of
 831 laboratory measured friction or cohesion for either intact rocks or their faulted equivalents (although data
 832 may exist in proprietary company records). Data for specific units of interest does exist, e.g., for the
 833 Oughtibridge Ganister, a seat earth in the Coal Measures (Rutter & Hadizadeh, 1991); and the Pennant
 834 Sandstone, a rare marine sandstone unit (Cuss et al., 2003; Hackston & Rutter, 2016), but a systematic
 835 analysis of the volumetrically dominant sandstone, siltstone and mudstone formations is notably absent.
 836 Instead, we use the measured dips of faults in the Coal Measures as a proxy for the coefficient of sliding
 837 friction, using the relationship

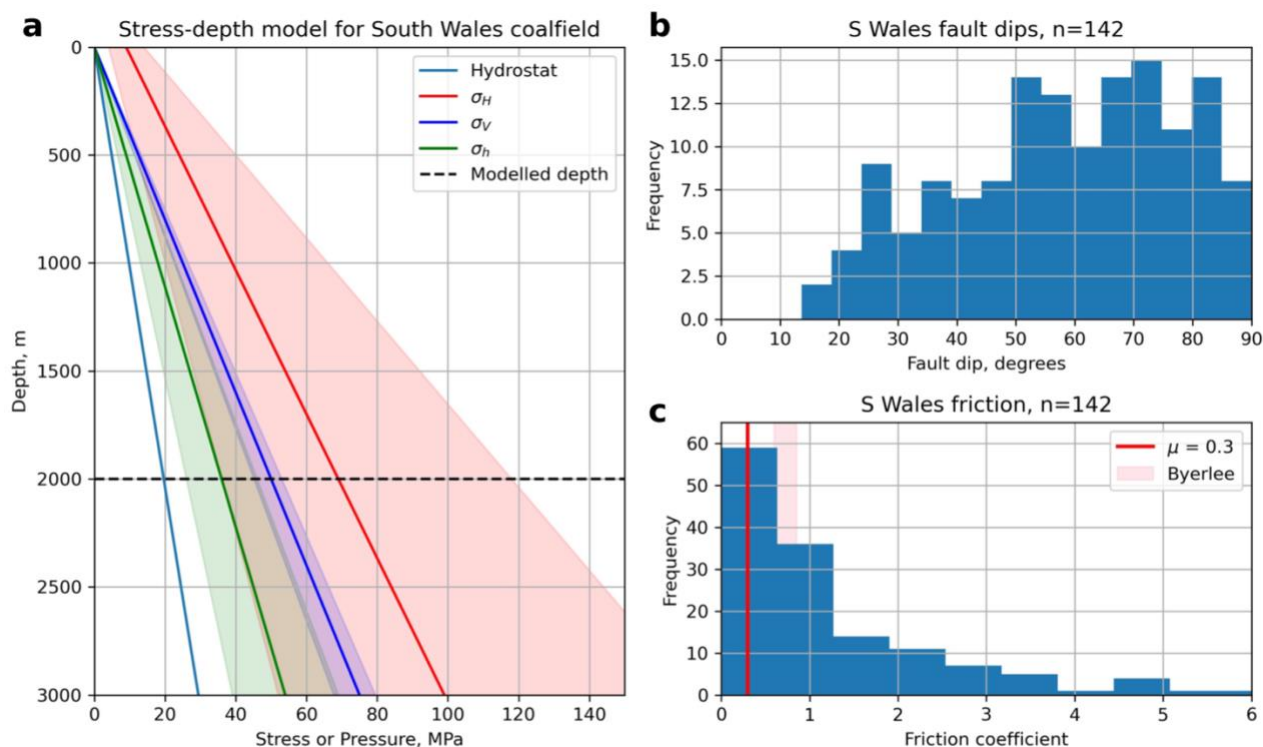
$$838 \quad \mu = 1/\tan(\pi - 2\beta) \quad (14)$$

839 where β is the angle between the fault plane and σ_1 at failure (Jaeger et al., 2009; Carvell et al., 2014). Such
 840 a calculation assumes Mohr-Coulomb failure and that the current dip of the fault is reasonably close to the
 841 dip at failure in the post-Westphalian deformation of the coalfields. For measured fault dips $< 45^\circ$, we assume
 842 that σ_1 was horizontal (Andersonian thrust/reverse fault regime) and for fault dips $\geq 45^\circ$ we assume σ_1 was
 843 vertical (Andersonian normal fault regime). In practice, some of these faults probably originated as strike-slip
 844 faults (i.e., with a sub-vertical dip and σ_2 vertical), and some of their dips have almost certainly been modified
 845 by compaction since their formation. However, this method of estimating the likely range of friction
 846 coefficients from measured dips remains simple to apply and useful to first order, in the absence of better
 847 data. From the dip data, the calculated friction coefficients vary between 0.0 and 6.0 for South Wales (Figures
 848 15b, c).



849 **Figure 14.** Maps of South Wales coalfield (a suggested site of shallow mine geothermal energy) showing:
 850 selected population centres (black squares); epicentres of seismicity (light blue dots; BGS catalogue –
 851 Musson, 1996); focal mechanisms (blue and white; Baptie, 2010); and orientations of the maximum
 852 horizontal stress (black lines; World Stress Map data – Heidbach et al., 2018). Inset equal area rose diagrams
 853 show orientations of mapped faults. Faults in the Coal Measures taken from the BGS Hydrogeological Map
 854 of South Wales (1:125k) ($n=3,408$), with a circular mean strike= 156° and a circular standard deviation= 65° .
 855

856 Based on the values of sliding friction calculated from measured fault dips across both coalfields a threshold
 857 stability value of $\mu=0.3$ is taken as a reasonable lower bound for faulted rock. This is the value used to
 858 compare with predicted slip tendencies calculated for each fault. For $T_s > 0.3$, the fault is deemed unstable,
 859 for $T_s \leq 0.3$ it is stable.



860

861 **Figure 15.** Constraints on input variables for the coalfield modelling of slip tendency. **a.** Stress-depth plot
 862 based on data from onshore UK (after Fellgett et al., 2018). Shaded areas show the extent of uncertainty in
 863 each stress. Also shown is the modelled depth of 2 km. **b-c.** Histograms of fault dips measured cross-sections
 864 on published BGS 1:50k maps of South Wales, and calculated values of friction coefficients derived from
 865 these dips assuming Mohr-Coulomb failure. Byerlee friction ($\mu=0.6-0.85$) shown as shaded pink box.
 866 Modelled critical values of friction ($\mu=0.3$) shown by red lines.

867

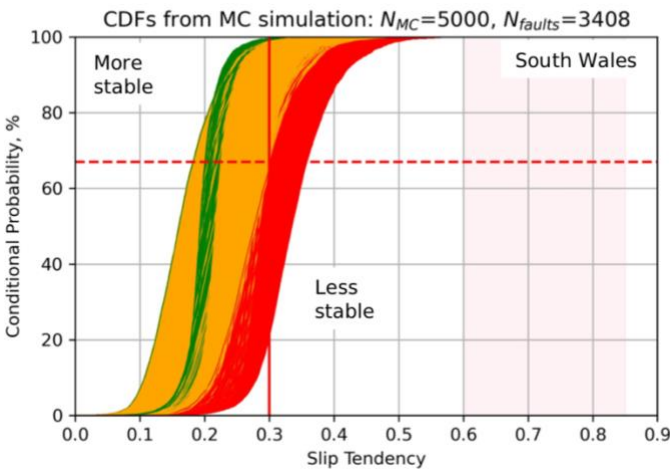
Variable	Mean	Standard deviation (κ for Von Mises)	Units	Distribution	Comments
South Wales coalfield T_s model, depth=2 km					
σ_v , vertical stress	50.0	3.75 (5% of mean)	MPa	Normal	Lithostatic for depth of 2 km, assuming average rock density of 2500 kg m ⁻³
σ_H , max. horizontal stress	70.0	14.0 (20% of mean)	MPa	Normal	After Fellgett et al., 2018
σ_h , min. horizontal stress	35.0	3.5 (10% of mean)	MPa	Normal	After Fellgett et al., 2018
Azimuth of σ_{Hmax}	160	$\kappa=200$	°	Von Mises (circular Normal)	After Fellgett et al., 2018; Baptie, 2010; WSM, 2016
Fault strike	-	-	°	As mapped	Digitised from BGS Hydrogeology sheet
Fault dip	-	$\kappa=25$ (based on measured dips from mapped sections)	°	Von Mises (circular Normal), truncated at 0 and 90	Fitted to data taken from cross-sections on BGS 1:50k sheets 229-231, 247-249, 263, 263

868

869 **Table 4.** Distributions of input variables used to model slip tendency (T_s) in the coalfield of South Wales.

870 Predictions of conditional probability for fault slip have been calculated for all faults in the coalfield using slip
871 tendency as the chosen measure: in the absence of detailed pore fluid pressure constraints or estimates of
872 cohesive strength, it is hard to justify modelling the fracture susceptibility. Slip tendency provides a first order
873 estimate of fault stability. A quadratic response surface was constructed for the coalfield using the full range
874 of measured fault strikes and dips, and the input variable distributions listed in Table 4 and constrained by
875 the data in Figure 15. Monte Carlo simulations ($N_{MC}=5,000$) were run for each mapped fault segment with
876 the other input variables drawn from their respective distributions.

877 Output CDFs for all faults are shown in Figure 16. For South Wales ($N=3,408$ faults), approximately 46% of
878 faults are predicted to have a 1 in 3 chance of being unstable (i.e., $T_s > 0.3$, shown in red), and 42% of faults
879 are predicted to have a 1 in 10 chance of being unstable (shown in amber).

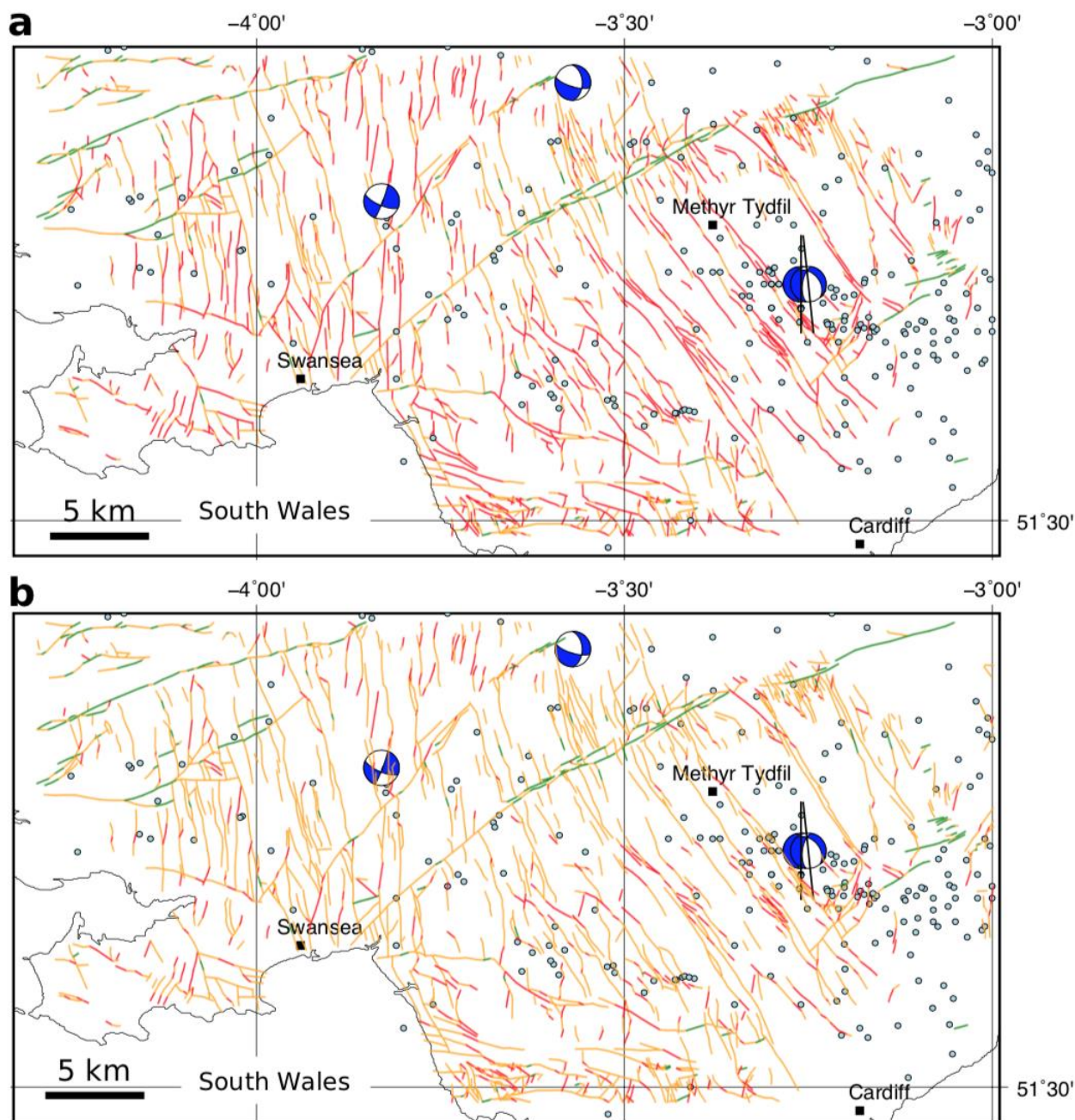


880

881 **Figure 16.** Output from the Monte Carlo modelling of slip tendency (T_s) in South Wales coalfield, UK. For slip
882 tendency, more stable faults skew towards the left (low T_s), less stable faults skew to the right (high T_s). CDFs
883 of predicted slip tendency for each mapped fault in South Wales. Colour coding of CDFs – red: >33% chance
884 of exceeding threshold friction ($\mu=0.3$, vertical red line), amber: >1% and <33% chance, green: < 1% chance.
885 Range of Byerlee friction shown by pink shading.

886 The results from the RSM/MC modelling shown in the CDFs are replicated in map view in Figure 17. Each
887 fault segment is colour coded using the same heuristic applied in the CDF: red faults have a conditional
888 probability of at least 33% of their slip tendency exceeding the chosen threshold value of fault rock friction
889 ($\mu=0.3$), amber (orange) faults have a 1-33% chance, and green faults have a less than 1% chance of being
890 unstable.

891 For South Wales, the general pattern of the predictions is consistent with the recorded focal mechanisms
892 (Figure 17a). The most likely fault segments to slip (coloured red) are those oriented either NNW/SSE or N/S,
893 corresponding with one of the nodal planes in each of the focal mechanisms. Faults trending ENE/WSW, such
894 as the Neath Disturbance, are predicted to have low probability of slip in the modelled stress regime (green).
895 Note that the Swansea Valley Disturbance trends ENE/WSW as a fault zone, but the constituent fault
896 segments are variously oriented including elements that trend NE/SW, and these are marked in red (high
897 probability of slip). Blenkinsop et al. (1986) noted that this fault zone may in fact have a shallow dip at depth,
898 which is not covered by the dip distribution used in our modelling, so further work is required here. The
899 location with the most recorded events lies to the SE of Merthyr Tydfil, and this corresponds to an area with
900 many mapped faults trending NW/SE marked with a high probability of slip, and consistent with two of the
901 focal mechanisms.



902

903 **Figure 17.** Output from the Monte Carlo modelling of slip tendency (T_s) in South Wales coalfield. **a.** Colour-
 904 coded fault map showing conditional probability of slip for each mapped fault. This map shows the
 905 unweighted values, as shown on the CDFs in Figure 14a. **b.** Colour-coded fault map showing conditional
 906 *weighted* probability of slip for each mapped fault. The weighted probability is calculated by multiplying the
 907 probability from the CDF in Figure 14a by the normalised fault smoothness, ranging from 1.0 for a perfectly
 908 straight (i.e., smooth) fault, and tending to 0.0 for a rough fault. Colour coding of CDFs – red: >33% chance
 909 of exceeding threshold friction ($\mu=0.3$), amber: >1% and <33% chance, green: < 1% chance.

910

911

912 Discussion

913 *Stress, pressure, and temperature*

914 The simulations described in this paper all critically depend on our knowledge of the *in situ* stress tensor. We
 915 can constrain some of the components of this tensor better than others. The vertical stress (σ_v) is usually the
 916 best constrained, a reflection of its derivation from the borehole density logs sampled at sub-metre
 917 resolution. Our estimates of the horizontal stresses, σ_{Hmax} and σ_{Hmin} , remain poorly constrained. Even in cases
 918 with relatively good data, e.g., from borehole leak-off tests (LOTs) and formation integrity tests (FITs), the
 919 “data density” for these stress components is generally sparse (compared to σ_v), and we are stuck with
 920 significant uncertainties. And these uncertainties matter, as shown by this study and previous work (e.g.,
 921 Chiaramonte et al., 2008; Walsh & Zoback, 2016). The fundamental dependence of shear failure on
 922 differential stress inherent in the Mohr-Coulomb failure criterion is reflected in the high ranking of stress
 923 tensor components in the tornado plots shown in this study. Also, larger uncertainties in stress components
 924 mean that the Andersonian regime may flip from the default “average” assumption to another orientation:
 925 e.g., an apparently strike-slip regime may in fact include a significant proportion of normal fault possibilities
 926 (>20% in the case of the Porthtowan Fault Zone shown here). One way to improve our knowledge of the
 927 stress tensor, and especially the azimuth of σ_{Hmax} would be to exploit richer catalogues of seismicity to
 928 produce more focal mechanisms for natural or induced events. Most countries would benefit from better –
 929 i.e., more widespread and higher resolution – continuous seismic monitoring. While this may be expensive
 930 with top of the range broadband equipment, citizen science devices, such as the Raspberry Shake, offer a
 931 low cost and viable alternative (Cochran, 2018; Anthony et al., 2019; Hicks et al., 2021; Holmgren & Werner,
 932 2021). Our study shows how Raspberry Shake data are effective for computing focal mechanisms. Analysis
 933 of more events would allow stress inversions to be performed on the data measured by these devices,
 934 especially when they are combined in *ad hoc* arrays to improve signal to noise ratios.

935 Pore fluid pressures at depth are also poorly known, even for a country like the UK with a long tradition of
 936 geological (and geophysical) science and rich history of mining and drilling into the crust. Most importantly,
 937 our knowledge of measured *in situ* pore fluid pressures in and around fault zones is generally poor.
 938 Theoretical predictions and model simulations abound, but direct measurements of this key parameter are
 939 almost non-existent. We need to know the actual limits of pore fluid pressures in fault zones, and their likely
 940 spatial and temporal variation over a fault plane throughout the seismic cycle. The situation is complicated
 941 by the finer scale structure of fault zones. Fault zones in low porosity and/or crystalline rocks (such as granite)
 942 can be divided into one or more narrow cores defined by fine grained fault rocks (gouges, cataclasites)
 943 surrounded by wider damage zones of more or less fractured rock. Permeability may be low in and across
 944 the core(s) and higher in the damage zones (Caine et al., 1996; Faulkner et al., 2010). In high porosity and/or
 945 granular rocks (such as sandstone), fault zones may be simpler, with fine grained fault rocks along narrow
 946 fault planes forming an effective fluid seal (Wibberley et al., 2008) These differences in the physical
 947 characteristics of the fault zones have consequences for the distribution of dynamic pore fluid pressures,
 948 which remain poorly known in detail.

949 The work described in this paper has ignored the effects of temperature. However, thermoelastic stress may
 950 be more important than poroelastic stress by a factor of 10 (Jacquey et al., 2015). In short, colder injected
 951 water may increase the chance of slip on a given fault. In the UK, our knowledge of the subsurface
 952 temperature field is increasing (Beamish & Busby, 2016; Farr et al., 2021), but we need more data, and again,
 953 especially from faulted rocks.

954 *Faults*

955 An implicit assumption in all of the modelling performed in this paper (and many others) is that we know
 956 something about the fault which may slip: i.e., we can only quantify risk on known faults. There will, in
 957 general, be many more unmapped faults in the subsurface, and these may be the ones most likely to slip due
 958 to a change in loading (of either *in situ* stress or fluid pressure). This is apparent in the maps for the coalfields
 959 shown in this paper in terms of the relative lack of correspondence between the surface mapped fault traces
 960 and the locations of recorded earthquakes. Some of this “mismatch” could be explained by the dip of the
 961 faults measured at the surface, but not all. Moreover, there are areas of apparently intense surface faulting
 962 and no recorded seismicity, and vice versa (recorded seismicity but no mapped surface faults). Some advance
 963 could be made to address this problem with the recognition that each recorded seismic event documents a
 964 fault plane, assuming that a double couple focal mechanism implies fault slip rather than dilation from dyke

965 emplacement or other mechanisms. And therefore the 3D position of each focal mechanism points to at least
966 part of a subsurface fault. The challenge then lies in mapping these seismic event fault planes into a viable
967 fault network. Better data (i.e., higher spatial resolution and extending to smaller event magnitudes) from
968 more dense arrays of seismometers would help with this task, as for the refinement of stress estimates noted
969 above.

970 *Rock properties*

971 The importance of good data on rock properties has been emphasised above, in the Worked Example for
972 fracture susceptibility and in the case study for the Porthtowan Fault Zone. In general, we need more and
973 better data on coefficients of friction and cohesive strength, especially for the target formations of
974 decarbonisation operations. Moreover, we need data for the intact *and* faulted rocks. We also need better
975 constrained correlations among rock properties. A widely used method in oil and gas is to derive estimates
976 of friction coefficient and UCS from wireline log datasets measuring porosity, slowness (velocity) or elasticity
977 e.g., Chang et al., 2006. However, as noted by these authors, the correlations are strictly valid only for the
978 specific formations tested in the laboratory, and even then, the uncertainties remain large. A further issue is
979 the tendency to average wireline log derived estimates over a depth interval, when for most sections of crust
980 this is the direction in which rock properties are expected to vary most rapidly. The Porthtowan Fault Zone
981 example above highlighted another issue: the relative impact of cohesion and friction on the predicted
982 stability depends on the magnitude of the cohesion in relation to the shear stress on the fault. For low
983 cohesion values, the constraints on friction become much more important. We need systematic
984 investigations of frictional behaviour at low cohesive strength, and detailed systematic correlations among
985 rock properties, especially for faulted crystalline basement rocks.

986 Collecting more laboratory data is no panacea, evidenced by the well-aided concerns over how we up-scale
987 rock properties and behaviours from mm- and cm-sized samples to whole fault zones. But calibrations and
988 correlations from careful, systematic laboratory data remain the cornerstone of estimating the key *in situ*
989 values. An interesting new focus would be to explore the nature of the skewness in mechanical property
990 datasets: why should friction coefficients skew low, and cohesive strength skew high?

991 The utility of the Mohr-Coulomb criterion used in this paper is largely down to its mathematical simplicity,
992 i.e., linearity and only two parameters (friction and cohesion). Other criteria are perfectly viable and could
993 easily be added to the pfs Python code, but some other failure criteria lack a clear mapping between their
994 parameters and the mechanics of sliding on rock surfaces.

995 *Applicability of T_s , T_d and S_f for quantifying risk*

996 A valid question is to ask whether any of these widely used measures of fault stability are, in fact, useful in
997 practical terms at the scale of faults on maps. All three measures focus on the simplified mechanics of slip on
998 a specific fault plane, with a fixed orientation and with specific rock properties. But seismic hazard is not
999 isolated at the level of single fault planes. Faults occur in patterns or networks, more or less linked together.
1000 Geometrical factors may be more important than the specifics of either the *in situ* stress or the rock
1001 properties, at the scale of observation. The observational record shows that bigger fault zones are the sites
1002 of bigger earthquakes, and they are also the locus of most displacement in a given network. Conversely,
1003 smaller faults host smaller seismic events, and accrue less overall displacement (Walsh et al., 2001). To begin
1004 to address this issue, we can weight the conditional probabilities of slip for a specific fault segment by a
1005 dimensionless normalised factor derived from the total length of the fault: e.g., $w_{size} = l_s / l_t$ where l_s is fault
1006 segment length and l_t is fault trace length. An alternative, but related idea, is that of the relationship between
1007 fault smoothness (or inversely, roughness) and fault maturity, and therefore seismic hazard (Wesnousky et
1008 al., 1988; Wells & Coppersmith, 1994; Leonard, 2010). The most seismically active faults are not only, or
1009 necessarily, the largest ones in their network, but tend to be the smoothest or most connected, reflecting
1010 the coalescence of fault segments through time and the removal of asperities through repeated slip events
1011 (Stirling et al., 1996). Therefore, we can weight the conditional probabilities of slip by a dimensionless factor
1012 of smoothness: $w_{smooth} = l_{straight} / \text{sum}(l_s)$, where $l_{straight}$ is the straight line length between fault end points,
1013 which is 1.0 for a perfectly smooth fault with all segments parallel and connected, and tends to 0.0 for rough,
1014 complex fault traces. Examples of the effect of these smoothness weightings applied to the conditional

1015 probabilities are shown in Figure 17b for the South Wales coalfield faults. The net effect is to reduce the
1016 number of most risky faults (shown in red) by about half. These approaches are the subject of further work
1017 and testing.

1018

1019 **Summary**

1020 In this paper, we have described and explained the Response Surface Methodology and shown how it can be
1021 combined with a Monte Carlo approach to generate probabilistic estimates of fault stability using published
1022 measures of slip tendency, dilation tendency and fracture susceptibility. Simulations show that a quadratic
1023 response surface always generates a better fit to the input variables in comparison to a linear surface, at the
1024 cost of larger matrices (more computer memory) and longer run times. Worked examples to calculate T_s and
1025 S_f with synthetic input distributions show how the quadratic response surfaces vary for each input parameter.
1026 For slip and dilation tendency, the primary dependence is (as expected) on the maximum differential stress,
1027 and therefore the maximum and minimum principal stresses of the *in situ* stress tensor, with a lesser
1028 dependence on the fault orientation. For fracture susceptibility, the situation is more complex: if cohesion is
1029 relatively high, S_f is mainly dependent on the *in situ* stresses and cohesion. But if cohesion is low – quite likely
1030 in fault zones – then the dependence of S_f on friction is much more significant. This is a key finding: the
1031 relative sensitivity of the input variables on the response surface varies with the absolute value of the
1032 variables.

1033 Sensitivity tests were used to assess how the shapes of different input distributions affect the predictions of
1034 fault stability. Varying the spread of symmetric (normal, Gaussian) distributions of input variables has a
1035 significant effect on the predictions, and this mirrors the reality of uncertainties in, for example, the principal
1036 stresses in a standard geomechanical analysis. As noted above, the vertical stress is often well constrained
1037 and has a lower relative standard deviation (say, 5% of the mean) than either the maximum or minimum
1038 horizontal stresses (typically 15-20% of their mean value). The shape and spread of skewed (asymmetric)
1039 distributions of rock properties (friction and cohesion) is also important. The direction of skewness is
1040 described by the sign of the parameter α for the skewed normal distributions used in this paper to model
1041 variations in rock properties. Friction is modelled with a negative skewness towards lower values, whereas
1042 cohesion is modelled with positive skewness towards higher values, but systematic laboratory data are
1043 needed to verify these assumptions. This will require a statistically significant number of repeat tests for each
1044 property on quasi-identical samples of the same rock.

1045 Case studies of two different locations demonstrated how a probabilistic approach can provide a useful
1046 assessment of fault stability, including which of the input variables are the most important for a given
1047 combination of *in situ* stress, fault plane orientation and rock properties. This then enables greater focus on
1048 improving the estimates of the key variables, and the relationships between them. For the Porthtowan Fault
1049 Zone in Cornwall, the modelling in this paper shows that we need more data for, and a better understanding
1050 of the relationship between, coefficients of friction and cohesive strength, especially at low values of friction
1051 (i.e., less than the Byerlee range of 0.6-0.85) to be expected in fault zones. For the South Wales coalfield,
1052 model outputs show how predictions of fault stability can be weighted by a simple index of fault smoothness
1053 to begin to allow for the effects of geometrical weakening within the fault system as whole, rather than
1054 focusing on each individual fault plane taken in isolation.

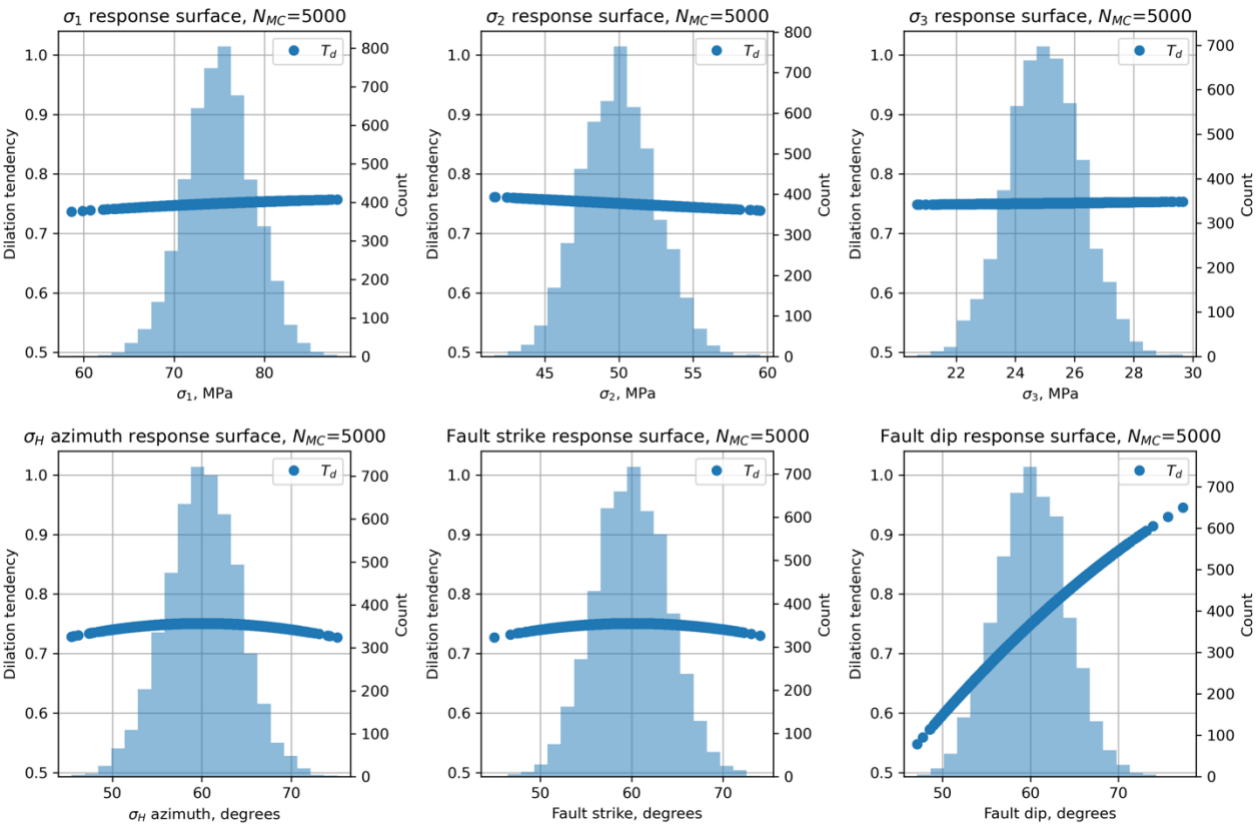
1055 It's obvious that uncertainty in the input parameters must translate into uncertainty in the output
1056 predictions. By combining a Response Surface Methodology with a Monte Carlo approach to the
1057 quantification of fault stability, we can explore, understand, and quantify how differing degrees of
1058 uncertainty among the input parameters feed through to uncertainty in the predicted stability measure.
1059 Response surfaces and tornado plots can help to identify which parameters are the most important in a
1060 particular analysis. Given our current state of knowledge of stress, fault orientations and fault rock
1061 properties, probabilistic estimates and iterative modelling are useful approaches to begin to de-risk the
1062 energy transition. Free, open source software to perform these analyses, such as the Python package pfs,
1063 can help to encourage their wider adoption and further refinement ("given enough eyeballs, all bugs are
1064 shallow"; Raymond, 2001). The deployment of abundant and relatively low-cost citizen science seismometers

1065 (e.g., Raspberry Shakes) could synergise two critical issues: the wider involvement of the public into open
1066 science debates about risk and the simultaneous collection of better data to constrain the local stress field.
1067 The energy transition and decarbonisation are urgent and essential tasks: we will only be successful if we
1068 manage to balance public perceptions of risk with the technical challenges inherent to the exploitation of
1069 faulted rock.

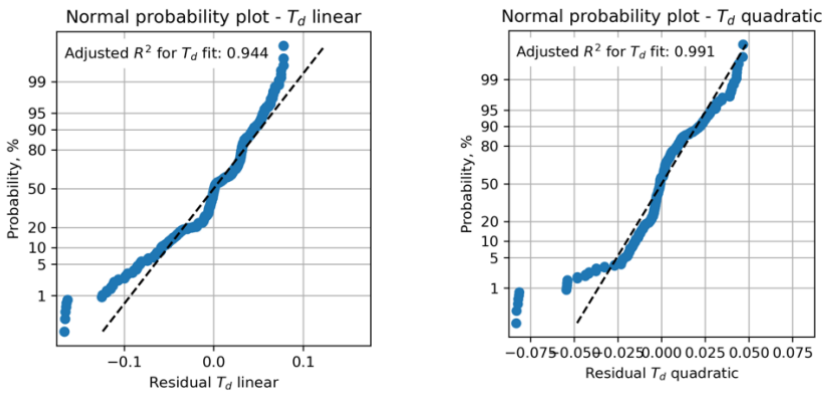
1070

1071 **Appendix A – Dilation tendency plots**

1072 For completeness, we include the analysis of dilation tendency (T_d) for the same synthetic input dataset used
1073 to calculate slip tendency (T_s) – i.e., input variable distributions taken from Table 2.



1074
1075 **Figure A1.** Histograms of input variables used to calculate dilation tendency T_d for the synthetic distributions
1076 shown in Table 2.



1077 **Figure A2.** Residual plots for linear and quadratic response surfaces for dilation tendency (T_d) using synthetic
1078 data. The quadratic fit has a higher value of the adjusted R^2 parameter and is therefore deemed better in this
1079 case.

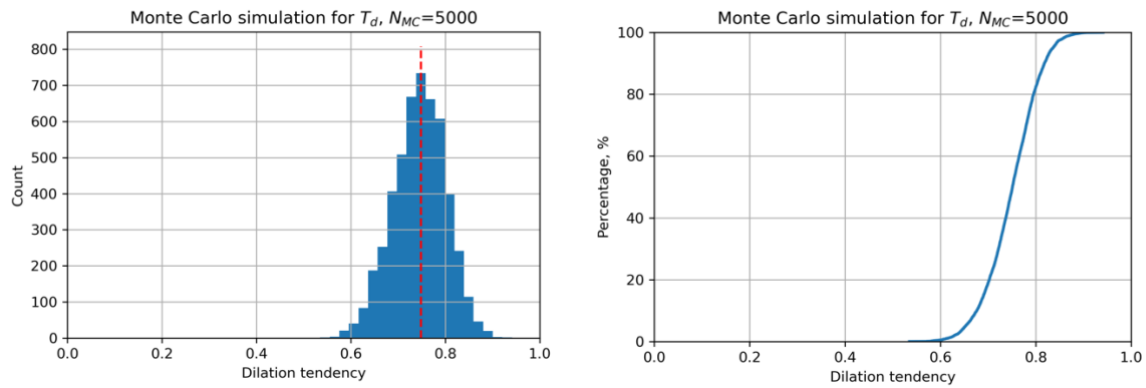


Figure A3. Output from Monte Carlo simulation ($N_{MC}=5,000$) of dilation tendency calculated using a quadratic response surface from synthetic input data. **a.** Histogram of calculated dilation tendency values, in this case showing a quasi-normal distribution with a mode of ~ 0.75 . **b.** Cumulative distribution function (CDF) of calculated dilation tendency values, showing the range in values from ~ 0.5 to ~ 0.9 .

Code availability

<https://github.com/DaveHealy-github/pfs>

Data availability

Author contribution

DH – 80%, SH – 20%. DH originated the study, wrote the code, ran the models. SH contributed seismology data and expertise, and contributed to the writing of the text.

Competing interests

The authors declare that they have no conflicts of interest.

Acknowledgements

DH first presented the core ideas in this paper at the Tectonic Studies Group AGM in Cardiff in 2014, and enjoyed discussions there with Dr Jonathan Turner (RWM Ltd). Thanks to former PhD student Dr Sarah Weihmann (now at BGR) and co-supervisor Dr Frauke Schaeffer (Wintershall DEA) for discussions about using oil industry wireline log data for quantifying geomechanical models. GMT (Wessel et al., 2013) was used for the maps. SciPy (Virtanen et al., 2021), Numpy (Harris et al., 2020), and matplotlib (Hunter, 2007) were used for the Python pfs code and Allmendinger et al. (2012) for various geomechanical and geometrical algorithms. We thank the reviewers for comments that improved the manuscript.

References

Alcalde, J., Bond, C.E., Johnson, G., Ellis, J.F. and Butler, R.W., 2017. Impact of seismic image quality on fault interpretation uncertainty. *GSA Today*.

- 1110 Allmendinger, R.W., Cardozo, N. and Fisher, D.M., 2011. Structural geology algorithms: Vectors and tensors.
1111 Cambridge University Press.
- 1112 Anderson, E.M., 1905. The dynamics of faulting. Transactions of the Edinburgh Geological Society, 8(3),
1113 pp.387-402.
- 1114 Anthony, R.E., Ringler, A.T., Wilson, D.C. and Wolin, E., 2019. Do low-cost seismographs perform well enough
1115 for your network? An overview of laboratory tests and field observations of the OSOP Raspberry Shake 4D.
1116 Seismological Research Letters, 90(1), pp.219-228.
- 1117 Ayash, S.C., Dobroskok, A.A., Sorensen, J.A., Wolfe, S.L., Steadman, E.N. and Harju, J.A., 2009. Probabilistic
1118 approach to evaluating seismicity in CO₂ storage risk assessment. Energy Procedia, 1(1), pp.2487-2494.
- 1119 Baptie, B., 2010. Seismogenesis and state of stress in the UK. Tectonophysics, 482(1-4), pp.150-159.
- 1120 Barcelona, H., Yagupsky, D., Vigide, N. and Senger, M., 2019. Structural model and slip-dilation tendency
1121 analysis at the Copahue geothermal system: inferences on the reservoir geometry. Journal of Volcanology
1122 and Geothermal Research, 375, pp.18-31.
- 1123 Batchelor, A.S. and Pine, R.J., 1986, August. The results of in situ stress determinations by seven methods to
1124 depths of 2500 m in the Carnmenellis granite. In ISRM International Symposium. OnePetro.
- 1125 Beamish, D. and Busby, J., 2016. The Cornubian geothermal province: heat production and flow in SW
1126 England: estimates from boreholes and airborne gamma-ray measurements. Geothermal Energy, 4(1), pp.1-
1127 25.
- 1128 Becker, A. and Davenport, C.A., 2001. Contemporary in situ stress determinations at three sites in Scotland
1129 and northern England. Journal of Structural Geology, 23(2-3), pp.407-419.
- 1130 Blenkinsop, T.G., Long, R.E., Kusznir, N.J. and Smith, M.J., 1986. Seismicity and tectonics in Wales. Journal of
1131 the Geological Society, 143(2), pp.327-334.
- 1132 Bond, C.E., 2015. Uncertainty in structural interpretation: Lessons to be learnt. Journal of Structural Geology,
1133 74, pp.185-200.
- 1134 Box, G.E., 1951. Wilson. KB [1951] On the Experimental Attainment of Optimum Conditions. Journal of the
1135 Royal Statistical Society, Series B (Methodological), 13(1), pp.1-45.
- 1136 Caine, J.S., Evans, J.P. and Forster, C.B., 1996. Fault zone architecture and permeability structure. Geology,
1137 24(11), pp.1025-1028.
- 1138 Carvell, J., Blenkinsop, T., Clarke, G. and Tonelli, M., 2014. Scaling, kinematics and evolution of a polymodal
1139 fault system: Hail Creek Mine, NE Australia. Tectonophysics, 632, pp.138-150.
- 1140 Chang, C., Zoback, M.D. and Khaksar, A., 2006. Empirical relations between rock strength and physical
1141 properties in sedimentary rocks. Journal of Petroleum Science and Engineering, 51(3-4), pp.223-237.
- 1142 Chiaramonte, L., Zoback, M.D., Friedmann, J. and Stamp, V., 2008. Seal integrity and feasibility of CO₂
1143 sequestration in the Teapot Dome EOR pilot: geomechanical site characterization. Environmental Geology,
1144 54(8), pp.1667-1675.
- 1145 Clarke, H., Verdon, J.P., Kettlety, T., Baird, A.F. and Kendall, J.M., 2019. Real-time imaging, forecasting, and
1146 management of human-induced seismicity at Preston New Road, Lancashire, England. Seismological
1147 Research Letters, 90(5), pp.1902-1915.
- 1148 Cochran, E.S., 2018. To catch a quake. Nature communications, 9(1), pp.1-4.
- 1149 CCC (UK Committee on Climate Change), 2019. Net Zero—Technical Report.

1150 Cuss, R.J., Rutter, E.H. and Holloway, R.F., 2003. The application of critical state soil mechanics to the
 1151 mechanical behaviour of porous sandstones. *International Journal of Rock Mechanics and Mining Sciences*,
 1152 40(6), pp.847-862.

1153 Das, D. and Mallik, J., 2020. Koyna earthquakes: a review of the mechanisms of reservoir-triggered seismicity
 1154 and slip tendency analysis of subsurface faults. *Acta Geophysica*, pp.1-16.

1155 Elsworth, D., Spiers, C.J. and Niemeijer, A.R., 2016. Understanding induced seismicity. *Science*, 354(6318),
 1156 pp.1380-1381.

1157 Farr, G., Sadasivam, S., Watson, I.A., Thomas, H.R. and Tucker, D., 2016. Low enthalpy heat recovery potential
 1158 from coal mine discharges in the South Wales Coalfield. *International Journal of Coal Geology*, 164, pp.92-
 1159 103.

1160 Farr, G., Busby, J., Wyatt, L., Crooks, J., Schofield, D.I. and Holden, A., 2021. The temperature of Britain's
 1161 coalfields. *Quarterly Journal of Engineering Geology and Hydrogeology*, 54(3).

1162 Faulkner, D.R., Jackson, C.A.L., Lunn, R.J., Schlische, R.W., Shipton, Z.K., Wibberley, C.A.J. and Withjack, M.O.,
 1163 2010. A review of recent developments concerning the structure, mechanics and fluid flow properties of fault
 1164 zones. *Journal of Structural Geology*, 32(11), pp.1557-1575.

1165 Fellgett, M.W., Kingdon, A., Williams, J.D. and Gent, C.M., 2018. Stress magnitudes across UK regions: New
 1166 analysis and legacy data across potentially prospective unconventional resource areas. *Marine and*
 1167 *Petroleum Geology*, 97, pp.24-31.

1168 Fellgett, M.W. and Haslam, R., 2021, April. Fractures in Granite: Results from United Downs Deep Geothermal
 1169 well UD-1. In *EGU General Assembly Conference Abstracts* (pp. EGU21-5593).

1170 Ferrill, D.A., Winterle, J., Wittmeyer, G., Sims, D., Colton, S., Armstrong, A. and Morris, A.P., 1999. Stressed
 1171 rock strains groundwater at Yucca Mountain, Nevada. *GSA Today*, 9(5), pp.1-8.

1172 Goebel, T.H.W., Rosson, Z., Brodsky, E.E. and Walter, J.I., 2019. Aftershock deficiency of induced earthquake
 1173 sequences during rapid mitigation efforts in Oklahoma. *Earth and Planetary Science Letters*, 522, pp.135-143.

1174 Green, A.S.P., Baria, R., Madge, A. and Jones, R., 1988. Fault-plane analysis of microseismicity induced by
 1175 fluid injections into granite. *Geological Society, London, Engineering Geology Special Publications*, 5(1),
 1176 pp.415-422.

1177 Hackston, A. and Rutter, E., 2016. The Mohr–Coulomb criterion for intact rock strength and friction—a re-
 1178 evaluation and consideration of failure under polyaxial stresses. *Solid Earth*, 7(2), pp.493-508.

1179 Hardebeck, J. L., & Shearer, P. M., 2002. A new method for determining first-motion focal
 1180 mechanisms. *Bulletin of the Seismological Society of America*, 92(6), 2264-2276.

1181 Harris, C.R., Millman, K.J., van der Walt, S.J., Gommers, R., Virtanen, P., Cournapeau, D., Wieser, E., Taylor,
 1182 J., Berg, S., Smith, N.J. and Kern, R., 2020. Array programming with NumPy. *Nature*, 585(7825), pp.357-362.

1183 Healy, D., Rizzo, R.E., Cornwell, D.G., Farrell, N.J., Watkins, H., Timms, N.E., Gomez-Rivas, E. and Smith, M.,
 1184 2017. FracPaQ: A MATLAB™ toolbox for the quantification of fracture patterns. *Journal of Structural Geology*,
 1185 95, pp.1-16.

1186 Heidbach, O., Rajabi, M., Cui, X., Fuchs, K., Müller, B., Reinecker, J., Reiter, K., Tingay, M., Wenzel, F., Xie, F.
 1187 and Ziegler, M.O., 2018. The World Stress Map database release 2016: Crustal stress pattern across scales.
 1188 *Tectonophysics*, 744, pp.484-498.

1189 Hennings, P.H., Lund Snee, J.E., Osmond, J.L., DeShon, H.R., Dommissie, R., Horne, E., Lemons, C. and Zoback,
 1190 M.D., 2019. Injection-induced seismicity and fault-slip potential in the Fort Worth Basin, Texas. *Bulletin of*
 1191 *the Seismological Society of America*, 109(5), pp.1615-1634.

1192 Hicks, S. P., Verdon, J., Baptie, B., Lockett, R., Mildon, Z. K., & Gernon, T., 2019. A shallow earthquake swarm
1193 close to hydrocarbon activities: Discriminating between natural and induced causes for the 2018–2019
1194 Surrey, United Kingdom, earthquake sequence. *Seismological Research Letters*, 90(6), 2095–2110.

1195 Hicks, S., Goes, S., Whittaker, A. C., & Stafford, P. J., 2021. Multivariate statistical appraisal of regional
1196 susceptibility to induced seismicity: application to the Permian Basin, SW United States. *Journal of*
1197 *Geophysical Research: Solid Earth. American Geophysical Union (AGU)*. DOI: 10.1029/2021jb022768

1198 Hincks, T., Aspinall, W., Cooke, R. and Gernon, T., 2018. Oklahoma's induced seismicity strongly linked to
1199 wastewater injection depth. *Science*, 359(6381), pp.1251-1255.

1200 Holmgren, J.M. and Werner, M.J., 2021. Raspberry Shake Instruments Provide Initial Ground-Motion
1201 Assessment of the Induced Seismicity at the United Downs Deep Geothermal Power Project in Cornwall,
1202 United Kingdom. *The Seismic Record*, 1(1), pp.27-34.

1203 Hunter, J.D., 2007. Matplotlib: A 2D graphics environment. *Computing in science & engineering*, 9(03), pp.90-
1204 95.

1205 IPCC, 2018. In: Masson-Delmotte, V., Zhai, P., Pörtner, H.O., Roberts, D., Skea, J., Shukla, P.R., Pirani, A.,
1206 Moufouma-Okia, W., Péan, C., Pidcock, R. and Connors, S., 2018. Global warming of 1.5 C. An IPCC Special
1207 Report on the impacts of global warming of, 1, pp.1-9.

1208 Jaeger, J.C., Cook, N.G. and Zimmerman, R., 2009. *Fundamentals of rock mechanics*. John Wiley & Sons.

1209 Jacquey, A.B., Cacace, M., Blöcher, G. and Scheck-Wenderoth, M., 2015. Numerical investigation of
1210 thermoelastic effects on fault slip tendency during injection and production of geothermal fluids. *Energy*
1211 *Procedia*, 76, pp.311-320.

1212 Kingdon, A., Fellgett, M.W. and Williams, J.D., 2016. Use of borehole imaging to improve understanding of
1213 the in-situ stress orientation of Central and Northern England and its implications for unconventional
1214 hydrocarbon resources. *Marine and Petroleum Geology*, 73, pp.1-20.

1215 Ledingham, P., Cotton, L. and Law, R., 2019, February. The united downs deep geothermal power project. In
1216 *Proceedings of the 44th Workshop on Geothermal Reservoir Engineering*, Stanford University, Stanford, CA,
1217 USA (pp. 11-13).

1218 Leonard, M., 2010. Earthquake fault scaling: Self-consistent relating of rupture length, width, average
1219 displacement, and moment release. *Bulletin of the Seismological Society of America*, 100(5A), pp.1971-1988.

1220 Li, X., Main, I. and Jupe, A., 2018. Induced seismicity at the UK 'hot dry rock' test site for geothermal energy
1221 production. *Geophysical Journal International*, 214(1), pp.331-344.

1222 Lisle, R.J. and Srivastava, D.C., 2004. Test of the frictional reactivation theory for faults and validity of fault-
1223 slip analysis. *Geology*, 32(7), pp.569-572.

1224 McLennan, D., Noble, S., Noble, M., Plunkett, E., Wright, G. and Gutacker, N., 2019. *The English indices of*
1225 *deprivation 2019: Technical report*.

1226 Miocic, J.M., Johnson, G. and Bond, C.E., 2019. Uncertainty in fault seal parameters: implications for CO₂
1227 column height retention and storage capacity in geological CO₂ storage projects. *Solid earth*, 10(3), pp.951-
1228 967.

1229 Moeck, I., Kwiatak, G. and Zimmermann, G., 2009. Slip tendency analysis, fault reactivation potential and
1230 induced seismicity in a deep geothermal reservoir. *Journal of Structural Geology*, 31(10), pp.1174-1182.

1231 Moos, D., Peska, P., Finkbeiner, T. and Zoback, M., 2003. Comprehensive wellbore stability analysis utilizing
1232 quantitative risk assessment. *Journal of Petroleum Science and Engineering*, 38(3-4), pp.97-109.

1233 Morris, A., Ferrill, D.A. and Henderson, D.B., 1996. Slip-tendency analysis and fault reactivation. *Geology*,
1234 24(3), pp.275-278.

- 1235 Musson, R.M., 1996. The seismicity of the British Isles. *Annals of Geophysics*, 39(3).
- 1236 Myers, R.H., Montgomery, D.C. and Anderson-Cook, C.M., 2016. Response surface methodology: process and
1237 product optimization using designed experiments. John Wiley & Sons.
- 1238 Nolan, L., 2016, July. The Welsh Index of Multiple Deprivation. In Presentation for the GSS Methodology
1239 Conference (Vol. 6).
- 1240 Pine, R.J. and Batchelor, A.S., 1984, October. Downward migration of shearing in jointed rock during hydraulic
1241 injections. In *International Journal of Rock Mechanics and Mining Sciences & Geomechanics Abstracts* (Vol.
1242 21, No. 5, pp. 249-263). Pergamon.
- 1243 Raleigh, C.B., Healy, J.H. & Bredehoeft, J.D., 1976. An experiment in earthquake control at Rangely, Colorado.
1244 *Science*, 191(4233), pp.1230-1237.
- 1245 Raymond, E., 2001. *The Cathedral & the Bazaar*, Revised Edition. O'Reilly.
- 1246 Reinecker, J., Gutmanis, J., Foxford, A., Cotton, L., Dalby, C. and Law, R. Geothermal exploration and
1247 reservoir modelling of the united downs deep geothermal project, Cornwall (UK). *Geothermics*, 97,
1248 p.102226, 2021.
- 1249 Roberts, J. J., Bond, C. E., & Shipton, Z. K., 2021. Fracking bad language—hydraulic fracturing and earthquake
1250 risks. *Geoscience Communication*, 4(2), 303-327.
- 1251 Rohmer, J. and Bouc, O., 2010. A response surface methodology to address uncertainties in cap rock failure
1252 assessment for CO₂ geological storage in deep aquifers. *International Journal of Greenhouse Gas Control*,
1253 4(2), pp.198-208.
- 1254 Rutter, E.H. and Hadizadeh, J., 1991. On the influence of porosity on the low-temperature brittle—ductile
1255 transition in siliciclastic rocks. *Journal of Structural Geology*, 13(5), pp.609-614.
- 1256 Sanchez, C., Saldi, G., Mitchell, T., Iacoviello, F., Meredith, P., Jones, A., Oelkers, E., and Striolo, A., 2020. The
1257 role of fluid chemistry on permeability and fault strength evolution in granite, EGU General Assembly 2020,
1258 Online, 4–8 May 2020, EGU2020-21850, <https://doi.org/10.5194/egusphere-egu2020-21850>
- 1259 Sanchez-Roa, C., Saldi, G.D., Mitchell, T.M., Iacoviello, F., Bailey, J., Shearing, P.R., Oelkers, E.H., Meredith,
1260 P.G., Jones, A.P. and Striolo, A., 2021. The role of fluid chemistry on permeability evolution in granite:
1261 Applications to natural and anthropogenic systems. *Earth and Planetary Science Letters*, 553, p.116641.
- 1262 Stephenson, M.H., Ringrose, P., Geiger, S., Bridden, M. and Schofield, D., 2019. Geoscience and
1263 decarbonization: current status and future directions. *Petroleum Geoscience*, 25(4), pp.501-508.
- 1264 Stirling, M.W., Wesnousky, S.G. and Shimazaki, K., 1996. Fault trace complexity, cumulative slip, and the
1265 shape of the magnitude-frequency distribution for strike-slip faults: A global survey. *Geophysical Journal*
1266 *International*, 124(3), pp.833-868.
- 1267 Streit, J.E. and Hillis, R.R., 2004. Estimating fault stability and sustainable fluid pressures for underground
1268 storage of CO₂ in porous rock. *Energy*, 29(9-10), pp.1445-1456.
- 1269 Townend, J. and Zoback, M.D., 2000. How faulting keeps the crust strong. *Geology*, 28(5), pp.399-402.
- 1270 Verdon, J.P. and Budge, J., 2018. Examining the capability of statistical models to mitigate induced seismicity
1271 during hydraulic fracturing of shale gas reservoirs. *Bulletin of the Seismological Society of America*, 108(2),
1272 pp.690-701.
- 1273 Virtanen, P., Gommers, R., Oliphant, T.E., Haberland, M., Reddy, T., Cournapeau, D., Burovski, E., Peterson,
1274 P., Weckesser, W., Bright, J. and Van Der Walt, S.J., 2020. SciPy 1.0: fundamental algorithms for scientific
1275 computing in Python. *Nature methods*, 17(3), pp.261-272.
- 1276 Walker, A., Baptie, B. and Ottemoller, L., 2003. UK earthquake monitoring 2002/2003.

1277 Walsh III, F.R. and Zoback, M.D., 2016. Probabilistic assessment of potential fault slip related to injection-
1278 induced earthquakes: Application to north-central Oklahoma, USA. *Geology*, 44(12), pp.991-994.

1279 Walsh, J.J., Childs, C., Meyer, V., Manzocchi, T., Imber, J., Nicol, A., Tuckwell, G., Bailey, W.R., Bonson, C.G.,
1280 Watterson, J. & Nell, P.A., 2001. Geometric controls on the evolution of normal fault systems. *Geological*
1281 *Society, London, Special Publications*, 186(1), pp.157-170.

1282 Wang, Q., Ru, Z., Zhao, R., Yu, C., Liu, Y. & Deng, S., 2020. A study on permeability along strike slip faults in
1283 Shunbei reservoir of Tarim Basin, China. *Energy Sources, Part A: Recovery, Utilization, and Environmental*
1284 *Effects*, pp.1-17.

1285 Wells, D.L. & Coppersmith, K.J., 1994. New empirical relationships among magnitude, rupture length, rupture
1286 width, rupture area, and surface displacement. *Bulletin of the seismological Society of America*, 84(4),
1287 pp.974-1002.

1288 Wesnousky, S.G., 1988. Seismological and structural evolution of strike-slip faults. *Nature*, 335(6188), pp.340-
1289 343.

1290 Wessel, P., Smith, W.H., Scharroo, R., Luis, J. and Wobbe, F., 2013. Generic mapping tools: improved version
1291 released. *Eos, Transactions American Geophysical Union*, 94(45), pp.409-410.

1292 Wibberley, C.A., Yielding, G. and Di Toro, G., 2008. Recent advances in the understanding of fault zone
1293 internal structure: a review. *Geological Society, London, Special Publications*, 299(1), pp.5-33.

1294 Williams, J.D., Fellgett, M.W. and Quinn, M.F., 2016. Carbon dioxide storage in the Captain Sandstone aquifer:
1295 determination of in situ stresses and fault-stability analysis. *Petroleum Geoscience*, 22(3), pp.211-222.

1296 Williams, J.D.O., Gent, C.M.A., Fellgett, M.W. and Gamboa, D., 2018. Impact of in situ stress and fault
1297 reactivation on seal integrity in the East Irish Sea Basin, UK. *Marine and Petroleum Geology*, 92, pp.685-696.

1298 Zhao, J., 1987. Experimental studies of the hydro-thermo-mechanical behaviour of joints in granite. Unpubl.
1299 PhD thesis, Imperial College, London, UK.

1300